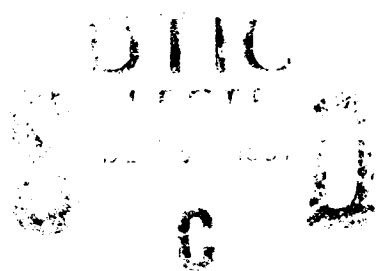


AFIT/GEO/ENG-91D-05

AD-A243 966



**PERFORMANCE ANALYSIS
of the
SPECKLE HOLOGRAPHY IMAGE
RECONSTRUCTION TECHNIQUE**

Thesis

Rudolf Neil VonNiederhausern, B.S.E.E
Major, USAF

AFIT/GEO/ENG-91D-05

Approved for public release; distribution unlimited.

91-19077



91 12 24 061

REPORT DOCUMENTATION PAGE

Form Approved
OMB No. 0704-0188

Public reporting burden for this collection of information is estimated to average 1 hour per response, including the time for reviewing instructions, searching existing data sources, gathering and maintaining the data needed, and completing and reviewing the collection of information. Send comments regarding this burden estimate or any other aspect of this collection of information, including suggestions for reducing this burden, to Washington Headquarters Services, Directorate for Information Operations and Reports, 1215 Jefferson Davis Highway, Suite 1204, Arlington, VA 22202-4302, and to the Office of Management and Budget, Paperwork Reduction Project (0704-0188), Washington, DC 20503.

1. AGENCY USE ONLY (Leave blank)		2. REPORT DATE December 1991	3. REPORT TYPE AND DATES COVERED Master's Thesis	
4. TITLE AND SUBTITLE Performance Analysis of Speckle Holography Image Reconstruction Technique			5. FUNDING NUMBERS	
6. AUTHOR(S) VonNiederhausern, Rudolf N., Major, USAF				
7. PERFORMING ORGANIZATION NAME(S) AND ADDRESS(ES) Air Force Institute of Technology, WPAFB OH 45433-6583			8. PERFORMING ORGANIZATION REPORT NUMBER AFIT/GEO/ENG-91D-05	
9. SPONSORING/MONITORING AGENCY NAME(S) AND ADDRESS(ES) Phillips Lab/ARCI Capt Michael Roggemann Kirtland AFB, NM 87117			10. SPONSORING/MONITORING AGENCY REPORT NUMBER	
11. SUPPLEMENTARY NOTES				
12a. DISTRIBUTION/AVAILABILITY STATEMENT Approved for public release; distribution unlimited			12b. DISTRIBUTION CODE	
13. ABSTRACT (Maximum 200 words) In speckle holography, short exposures frames along with wave front measurements allow post processing image reconstruction. With speckle holography the amplitude of high spatial frequencies is boosted to allow resolution out to the diffraction limit of the telescope. To provide system parameters for the wave front sensor design, a software analysis program has been developed that provides the system transfer function as a function of the number and size of sensor subapertures and sensor noise. Trends in the ratio of the atmospheric coherence diameter to wave front subaperture size and the effect on the system transfer function have been obtained. Data obtained with the system transfer function algorithm depicts the criticality of the ratio of r_0 (atmospheric coherence diameter) to the wave front sensor subaperture size. For a ratio of r_0 to subaperture size of 2 to 1, the amplitude of high spatial frequencies are boosted to nearly 70% of the amplitude of lower spatial frequencies.				
14. SUBJECT TERMS system transfer function, speckle holography, atmospheric compensation, optical transfer function, wave front analysis			15. NUMBER OF PAGES 71	
			16. PRICE CODE	
17. SECURITY CLASSIFICATION OF REPORT Unclassified	18. SECURITY CLASSIFICATION OF THIS PAGE Unclassified	19. SECURITY CLASSIFICATION OF ABSTRACT Unclassified	20. LIMITATION OF ABSTRACT UL	

PERFORMANCE ANALYSIS of the SPECKLE HOLOGRAPHY IMAGE RECONSTRUCTION TECHNIQUE

Thesis

Presented to the Faculty of the School of Engineering
of the Air Force Institute of Technology

Air University

In Partial Fulfillment of the
Requirements for the Degree of
Master of Science in Electrical Engineering

Rudolf Neil VonNiederhausern, B.S.E.E
Major, USAF

December, 1991

Approved for public release; distribution unlimited.

Preface

I wish to thank the Air Force Institute of Technology for the opportunity I had to attend and increase my understanding of light and its propagation through the atmosphere. Additionally my thesis advisor, Byron Welsh, was very instrumental in clarifying the problem of atmospheric compensation. He was typical of the faculty of the Air Force Institute of Technology, interested in insuring the students understand. I wish to thank my wife, Alice, and my children, Josef Rudolf, Sonia Marie, Tasha Lena, Michael Alma, Corinna Wilhelmina, Tanya Ada Anne, Bruce Albert, Hans William, and our son born during our time at AFIT, Samuel Orson named after the great indian Samuel for their support. My family has been very understanding and helpful in this work. I have enjoyed my assignment to the Air Force Institute of Technology.

Rudolf Neil VonNiederhausern

Table of Contents

Preface	ii
Table of Contents	iii
List of Figures	v
List of Tables	viii
Abstract	ix
I. Introduction	1-1
1.1 Background	1-1
1.2 Atmospheric Compensation Techniques	1-3
1.2.1 Adaptive Optics	1-3
1.2.2 Post Processing Image Reconstruction	1-5
1.3 Speckle Holography Image Reconstruction	1-5
1.3.1 Speckle Holography Image Reconstruction Technical Description	1-5
1.3.2 Military Benefits of Speckle Holography Image Reconstruction	1-7
1.3.3 Requirements for Performance Analysis of Speckle Holography Image Reconstruction	1-7
1.4 Sequence of Presentation	1-7
II Literature Review	2-1
2.1 Stellar Speckle Phenomena	2-1
2.2 Speckle Holography Image Reconstruction	2-3
2.2.1 Theory of Self Referenced Speckle Holography	2-7
2.2.2. Experiment Setup and Results	2-8
2.3 Speckle Holography Image Reconstruction Analysis	2-9

2.4	System Modelling	2-11
III	Analysis	3-1
3.1	System Models	3-1
3.2	System Transfer Function Algorithm Development	3-5
3.3	STF Numerical Analysis	3-12
IV	Results	4-1
4.1	Slope Measurement Noise	4-1
4.2	Wave Front Reconstructor	4-3
4.3	Phase-Structure Function	4-3
4.4	Aperture, Wave Front Sensor and Wave Front Reconstructor Description	4-3
4.5	Idealized Results	4-5
4.6	Expected Results	4-5
4.7	Variations in Photon Count	4-8
4.8	Variations in Ratio of Subaperture to Atmospheric Coherence Diameter	4-16
4.9	Variations in Number of Subapertures	4-19
4.10	System Spread Function	4-21
4.11	System Strehl Ratio	4-28
4.12	Performance Analysis of the Air Force Phillips Laboratory Compensation Experiment	4-32
V	Conclusions and Recommendations	5-1
5.1	Thesis Contributions	5-1
5.2	Key Elements	5-1
5.3	Additional Analysis	5-2
	Bibliography	A-1
	Vita	A-2

List of Figures

Figure	Page
1. Distortion of an image's wave front by atmospheric turbulence	1-2
2. Adaptive or active optics system	1-4
3. Speckle holography image reconstruction system	1-6
4. Short exposure narrow band photograph of a magnified image of an unresolved star taken with the 5 m Mount Palomar telescope (5:256)	2-2
5. Simplified atmospheric model of an instantaneous image through the atmosphere (5:260)	2-4
6. Schematic diagram of the speckle pattern from a bright binary star whose components have equal magnitude; the black dots indicate bright speckles and are paired (5:268)	2-5
7. Layout of self-referenced speckle holography instrument (2:4528)	2-6
8. Computer image of α Aurigae (Capella) image; (A) focal plane image; (B) atmospheric psf; (C) compensated image (2:4528) . .	2-10
9. Block diagram by J. Primot of the processing algorithm of the turbulence-degraded images to the object image restoration (6:1599)	2-12
10. Conjugate aperture and wave front sensor planes (7:1775) . . .	3-2
11. Conjugate aperture and wave front sensor planes (7:1775) . . .	4-4
12. System transfer function results for ideal case	4-6
13. System transfer function results for representative case . . .	4-7
14. STF for the subaperture photon count ranging from 10 to 800. Other parameters are constant, $D=2L$, and $L = 1/2 r_o$	4-9
15. STF for the subaperture photon count ranging from 10 to 800. Other parameters are constant, $D=2L$, and $L = 1 r_o$	4-10
16. STF for the subaperture photon count ranging from 10 to 800. Other parameters are constant, $D=2L$, and $L = 2 r_o$	4-11
17. STF for the subaperture photon count ranging from 10 to 800. Other parameters are constant, $D=2L$, and $L = 4 r_o$	4-12

18. STF for the subaperture photon count ranging from 10 to 400.
Other parameters are constant, $D=5L$, and $L = 1/2 r_0$ 4-13
19. STF for the subaperture photon count ranging from 10 to 400.
Other parameters are constant, $D=5L$, and $L = 1 r_0$ 4-14
20. STF for the subaperture photon count ranging from 10 to 800.
Other parameters are constant, $D=5L$, and $L = 2 r_0$ 4-15
21. STF for $L/r_0 = .1$ to 4. Other parameters are constant,
 $D=2L$, and photon count = 504-17
22. STF for $L/r_0 = .1$ to 2. Other parameters are constant,
 $D=5L$, and photon count = 504-18
23. STF for changes in the sensor configuration, $D= 2L, 3L, 4L$, and
 $5L$. Other parameters are constant, $r_0 = 1$, and photon
count = 1004-20
24. System spread function for the subaperture photon count ranging
from 10 to 800. Other parameters are constant, $D = 2L$, and
 $L = 1/2 r_0$ 4-22
25. System spread function for the subaperture photon count ranging
from 10 to 800. Other parameters are constant, $D = 2L$, and
 $L = 1 r_0$ 4-23
26. System spread function for the subaperture photon count ranging
from 10 to 800. Other parameters are constant, $D = 2L$, and
 $L = 2 r_0$ 4-24
27. System spread function for the subaperture photon count ranging
from 10 to 400. Other parameters are constant, $D = 5L$, and
 $L = 1/2 r_0$ 4-25
28. System spread function for the subaperture photon count ranging
from 10 to 400. Other parameters are constant, $D = 5L$, and
 $L = 1 r_0$ 4-26
29. System spread function for changing subaperture to r_0 ratio.
Other parameters are constant, $D = 5L$, and photon count = 50 .4-27
30. System Strehl ratio versus subaperture photon count. The other
parameters are constant, $D = 2L$, and $L = 1/2 \& 1 r_0$ 4-29
31. System Strehl ratio versus subaperture photon count. The other
parameters are constant, $D = 5L$, and $L = 1/2 \& 1 r_0$ 4-30
32. System Strehl ratio versus atmospheric coherence diameter r_0 .
Other parameters are constant $D = 5L$, and photon count = 50 .4-31

33. Squaring of imaging aperture and sensor configuration for the Air Force Phillips experiment performance analysis4-33
34. STF performance analysis of the Air Force Phillips experiment. Photon count is 1221 per subaperture. The L/r_0 is .1. A 5 x 5 sensor configuration was used to obtain the plotted data . . .4-34
35. SSF performance analysis of the Air Force Phillips experiment. Photon count is 1221 per subaperture. The L/r_0 is .1. A 5 x 5 sensor configuration was used to obtain the plotted data . . .4-35
36. STF performance analysis of the Air Force Phillips experiment. Photon count varies from 1 to 400 count per subaperture. The L/r_0 is .1. A 5 x 5 sensor configuration was used to obtain the plotted data4-36

List of Tables

Table	Page
I. STFnumerator Correlation Equivalence	3-10
II. STFdenominator Correlation Equivalence	3-11

Abstract

In speckle holography short exposure frames along with wave front measurements allows post processing image reconstruction. With speckle holography the amplitude of high spatial frequencies is boosted to allow resolution out to the diffraction limit of the telescope. To provide system parameters for the wave front sensor design, a software analysis program has been developed that provides the system transfer function as a function of the number and size of sensor subapertures and sensor noise. Trends in the ratio of r_0 (atmospheric coherence diameter) to wave front subaperture size and the effect on the system transfer function have been obtained. Data obtained with the system transfer function algorithm depicts the criticality of the ratio of r_0 to the wave front sensor subaperture size. For a ratio of r_0 to subaperture size of 2 to 1, the amplitude of high spatial frequencies are boosted to nearly 70% of the amplitude of the lower spatial frequencies.

PERFORMANCE ANALYSIS

of the

SPECKLE HOLOGRAPHY IMAGE

RECONSTRUCTION TECHNIQUE

I. Introduction

1.1 Background

The resolution of long exposure uncompensated optical systems designed to image exo-atmospheric or space objects is ultimately limited by atmospheric turbulence. Turbulence causes random phase fluctuations in the light wave propagating through the atmosphere. Atmospheric turbulence is caused by the non-uniform heating of pockets of air. These pockets of air or turbulent eddies distort the wave front of the image of the space object as it passes through the atmosphere (see fig. 1). For large telescopes (i.e., 1-3 meters in diameter), turbulence limits resolution to that obtainable by a telescope of diameter r_0 , where r_0 is the atmospheric coherence diameter. At the best sites in the world, seeing conditions are such that r_0 ranges from 10 to 30 cm. Atmospheric turbulence restricts the angular resolution of imaging systems operating at visible wavelengths to at best 1 arc second. To better exploit space, it is imperative to be able to resolve space objects of interest to greater detail than currently possible with conventional ground telescopes.

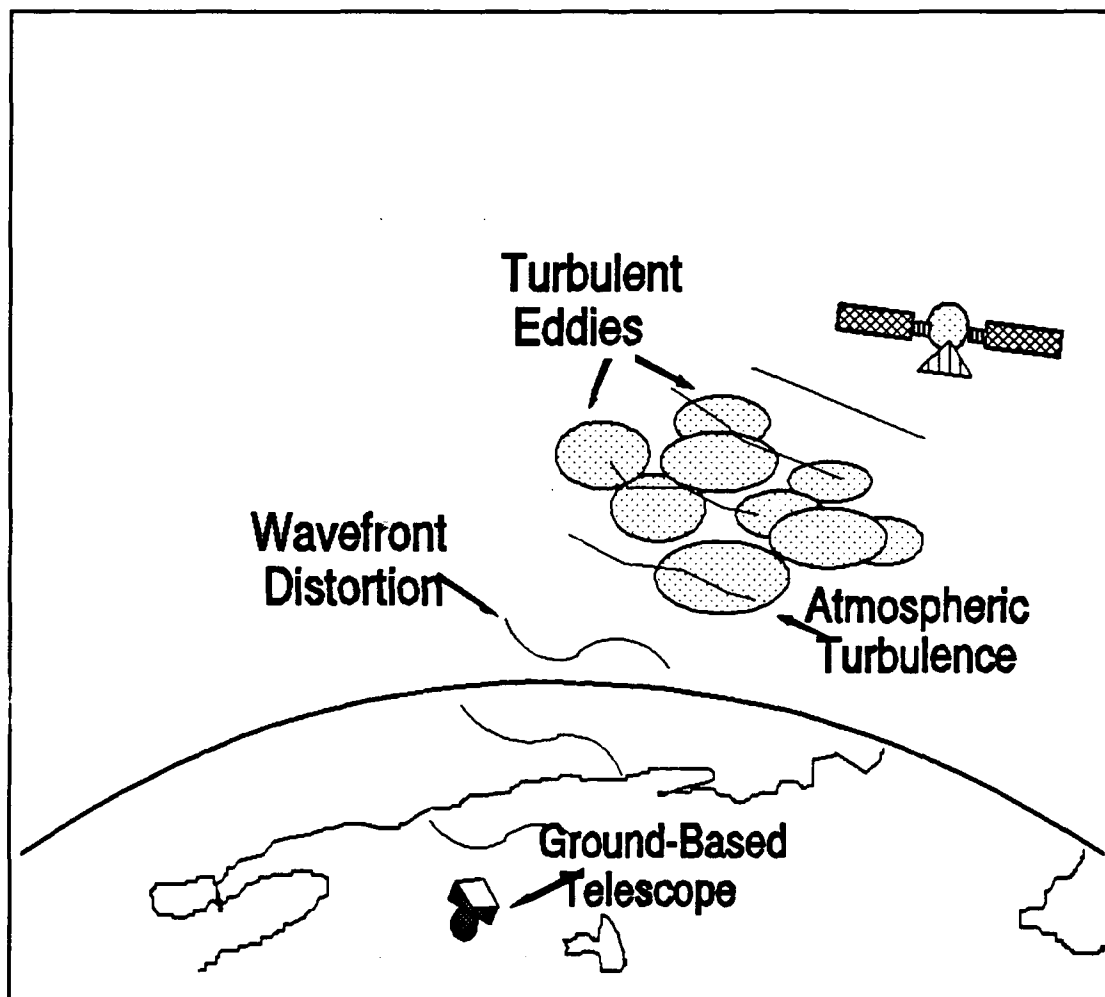


Fig. 1 Distortion of an image's wave front by atmospheric turbulence.

1.2 *Atmospheric Compensation Techniques*

The techniques used to compensate for degradation caused by atmospheric turbulence can be separated into two broad categories. The two categories are real time systems using adaptive optics and post-processing systems using extensive computer processing.

1.2.1 Adaptive Optics: The first compensation category is adaptive or active optics. In adaptive or active optics, the system compensates in real time for distortions in the image's wave front. John Hardy defines active optics as a general term for optical components whose characteristics are controlled in real time to modify optical wave fronts. The simplest active optical systems are those controlling focus and tilt and range in complexity up to systems employing deformable mirrors which may possess more than a hundred degrees of freedom. Three basic components of an optical system are required: a wave front modifying device, which may be reflective or refractive; a measuring device which accepts light and provides an output related to the property being optimized; and an information/processing device which accepts the measured data and converts it into the appropriate control signals for the wave front modifying device (1:651).

In an active optics system the incoming distorted wave front is passed from a deformable mirror to a beam splitter (see fig. 2). Part of the wave front energy is used by a wave front sensor to measure the wave front gradient. The gradient data from the wave front sensor is provided to the control system which in turn issues commands to the deformable mirror correcting for the distortion. In a closed loop scenario, the deformable mirror, the wave front sensor and the controls reduce the distortion. The image quality of the object passed through and active optics system is greatly improved. Additionally, since the compensation occurs in the millisecond range, distortions are canceled in real time.

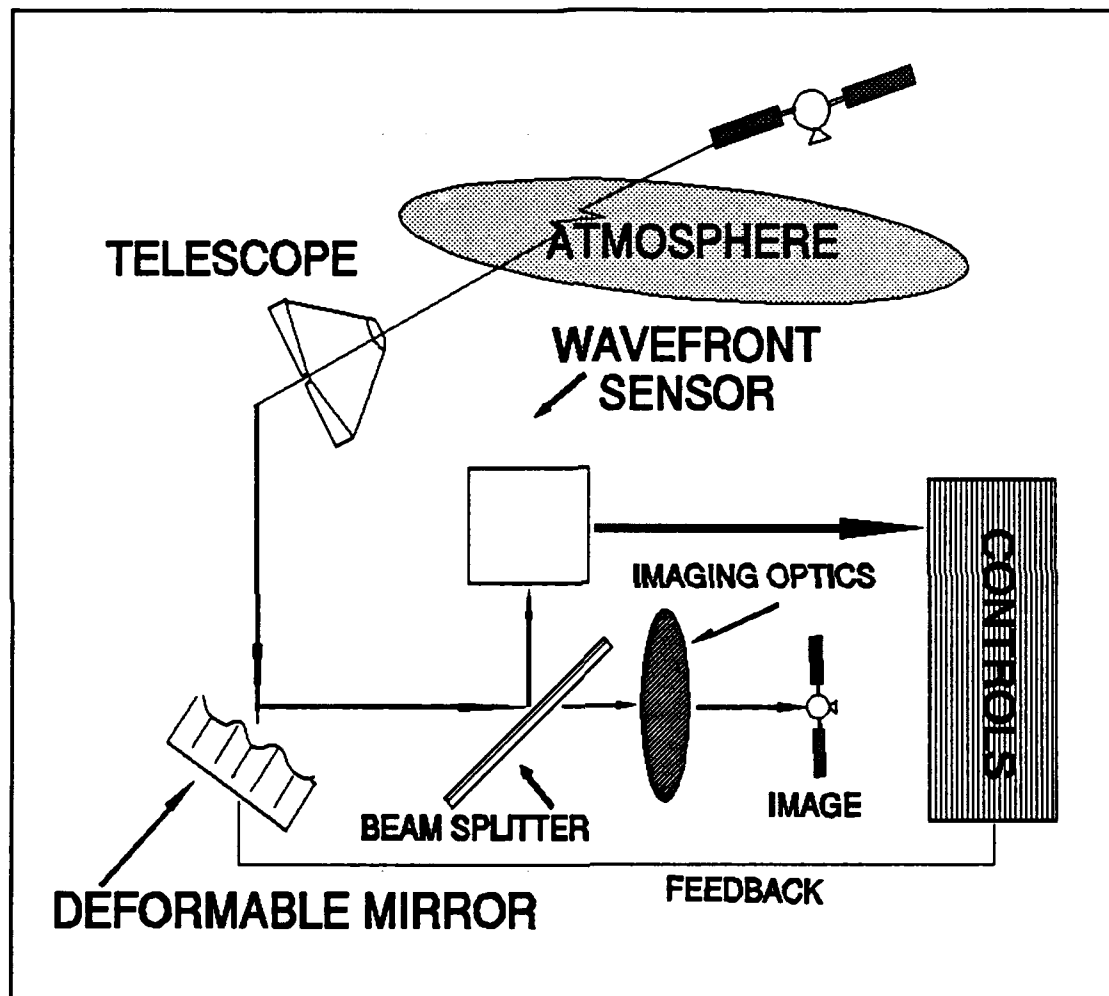


Fig. 2 Adaptive or active optics system.

1.2.2 Post Processing Image Reconstruction: In the second category, the distorted wave front is recorded in the image plane using a short exposure time. Extensive computer processing techniques are then used to reconstruct an estimate of the distortion free image.

1.3 *Speckle Holography Image Reconstruction*

1.3.1 Speckle Holography Image Reconstruction Technical Description: The speckle holography image reconstruction technique combines aspects of both compensation categories of above. In speckle holography the wave front sensor is retained, but the actual compensation is performed after recording the distorted image (see fig. 3). For speckle holography, simultaneous records of the image data and wave front gradients are obtained. The camera in the diagram obtains short exposure images while the wave front sensor obtains the wave front gradients. These simultaneous records are provided to the computer. From the wave front sensor data an estimate of the atmospheric transfer function is developed. A compensated image is then produced through a digital deconvolution (2:4527).

1.3.2 Military Benefits of Speckle Holography Image Reconstruction:

The ability to see through the atmosphere into space has not only scientific benefits for astronomy, but military benefits as well. To assess the state of health of space objects it is imperative to obtain clear and detailed images of the object of interest. The United State Air Force is interested in techniques to compensate for atmospheric turbulence. Paraphrasing Col L. John Otten (Commander, Air Force Weapons Laboratory, 1989). "Atmospheric compensation issues are similar for projecting or collecting light, although the telescope (referring to a new high-resolution telescope located at the Starfire Optical Range, Kirtland Air Force Base, New Mexico) will not be capable of projecting power into space. Ground-based lasers for strategic defense require atmospheric compensation techniques as do directed energy anti-satellite weapons" (3:47). Atmospheric

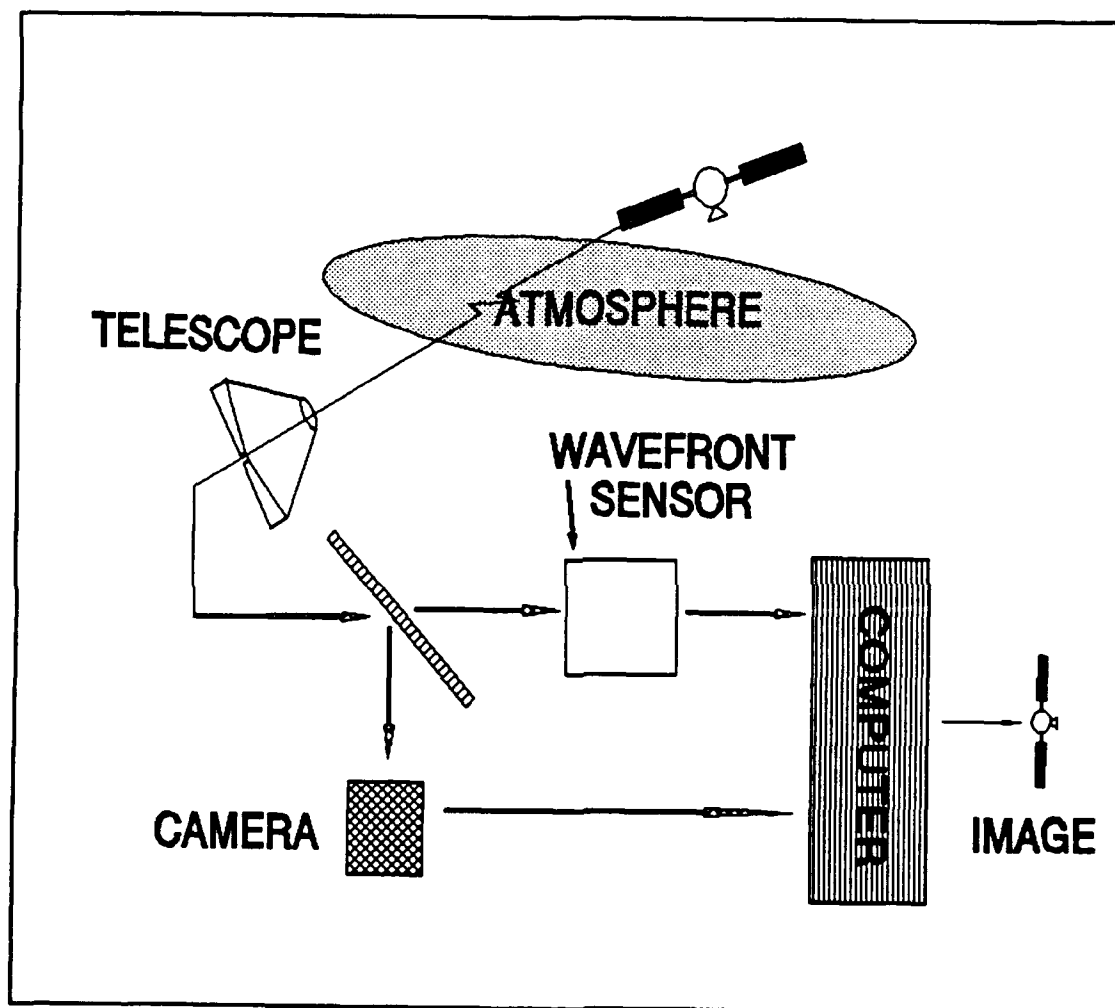


Fig. 3 Speckle holography image reconstruction system.

compensation will improve the military mission. With improvements in speckle holography image reconstruction enhanced images of space objects will be possible.

1.3.3 Requirements for Performance Analysis of Speckle Holography Image Reconstruction:

Within the last two years the Air Force Phillips Laboratory has been successful in obtaining enhanced images of stars using speckle holography image reconstruction (2:4528). These achievements are evidence of the potential of speckle holography image reconstruction for not only astronomical observations but military observations as well. However, an optimized speckle holography image reconstruction system similar to the one developed by the Air Force Phillips Laboratory requires tradeoffs studies. These trade offs involve numerous parameters. Of these parameters, the brightness of the object of interest determines the image intensity and the number of photons available for the wave front sensor. The size of the wave front sensor subapertures also determines the number of photons available per subaperture and sets the corresponding ratio of the subaperture size to the atmospheric coherence diameter, r_0 . To investigate the subaperture size versus photon count, this thesis work sought to address in depth these two variables and define their impact on a speckle holography image reconstruction system.

1.4 *Sequence of Presentation*

Chapter II provides the literature research. Chapter III presents the analysis and algorithm development. Chapter IV presents the results while Chapter V presents the summary and recommendations.

II Literature Review

Several articles have been written on the stellar speckle phenomena and on speckle holography image reconstruction. To understand the basics of stellar speckle phenomena this thesis will review a report by Christopher Dainty (5:255-280). To review speckle holography image reconstruction, a synopsis of the experiment report by the Air Force Phillips Laboratory will be presented (2:4517-4529). And finally, to provide for the basis of the performance analysis of speckle holography image reconstruction, this thesis will review a report by J. Primot (6:1598-1608).

2.1 Stellar Speckle Phenomena

Prior to defining speckle holography image reconstruction and the performance analysis of a system that performs post image reconstruction, this thesis will present a synopsis of the stellar speckle phenomena. Christopher Dainty in his report brings to light that the speckle phenomena has been known since the days of Newton but he reiterates that it was the invention of the laser that permitted in-depth analysis of speckle. He further defines stellar speckle interferometry as the technique for obtaining diffraction limited resolution of stellar objects despite the presence of a turbulent atmosphere. The basic principles of stellar interferometry presented follows closely Dainty's presentation.

In his observations of a short exposure (10 milliseconds) photograph of a star (fig. 4), Dainty presents that the highly magnified image has a speckle-like structure. He observed the speckle size has the same order of magnitude as the Airy disc of the telescope. He also stated that the long exposure image was simply composed of the sum of many short exposure images each with a speckle structure that has different detail, and was therefore a smooth intensity distribution whose diameter was approximately one arc second in good seeing for a 5 m telescope. The minimum speckle size on the other hand was approximately 0.02 arc seconds for a 5 m telescope. By extracting correctly the information in short exposure pictures of objects with more than one resolvable element, detail can

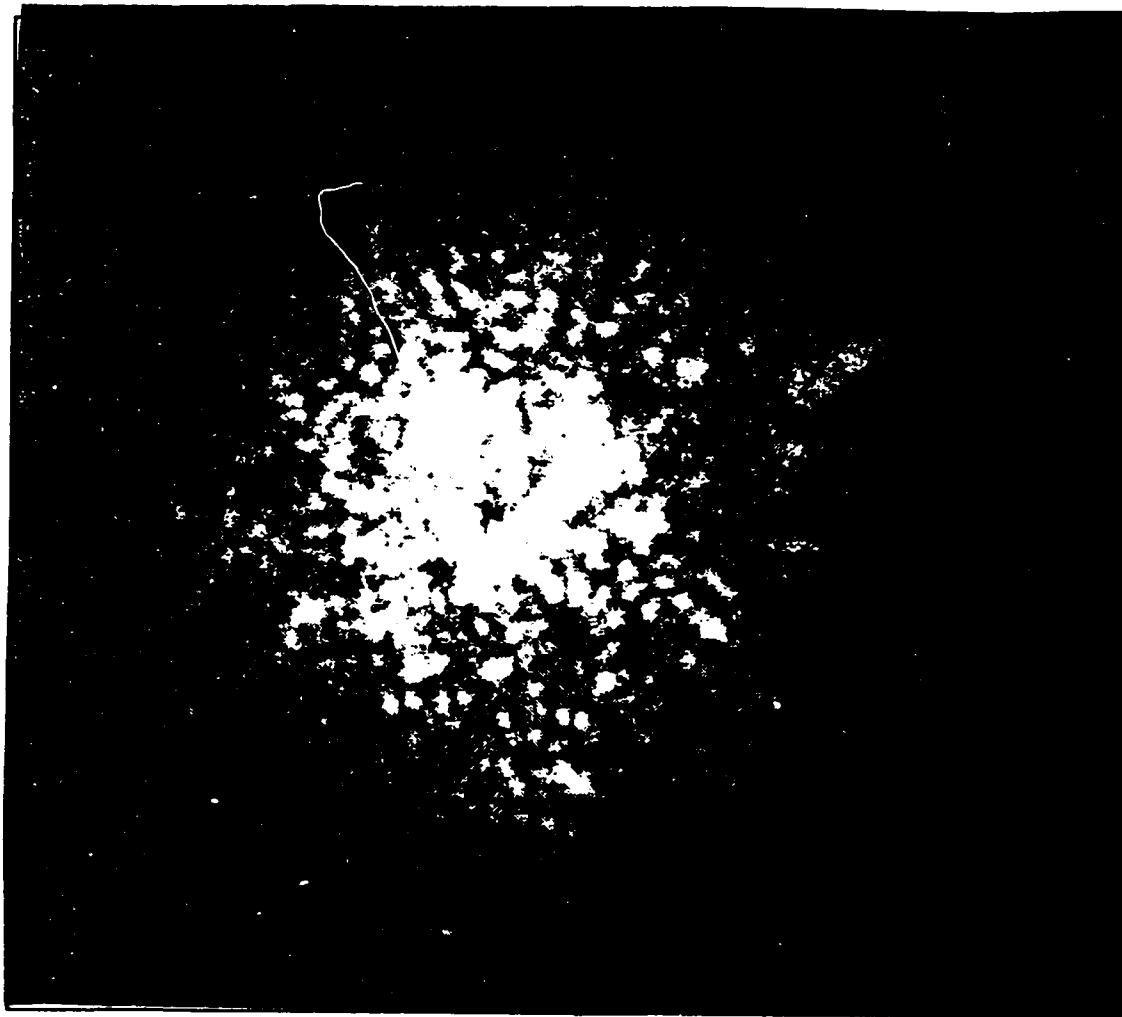


Fig. 4 Short exposure narrow band photograph of a magnified image of an unresolved star taken with the 5 m Mount Palomar telescope (5:256).

be observed down to the diffraction limit of the telescope (5:256).

Dainty also provides a simple atmospheric model (fig. 5) of the effect of the atmosphere on the image of a star (5:260-270). The star is essentially a point source. Due to the great distance of the star, the wave front is planar at the onset of the earth's atmosphere. As the wave front propagates through the turbulent atmosphere distortion occurs. The instantaneous image of the star is distributed over the image field. For a point source such as a star this instantaneous image is the point spread function of the combined telescope and turbulent atmosphere. To further demonstrate the stellar speckle phenomena, Dainty presents the simplified speckle diagram of a bright binary star (fig. 6) (5:269). The twin stars are marked 1 and 2 in the diagram. The speckles are paired or duplications of the twin dots marked 1 and 2. The spot size of the dots will be the size of the airy disk of the unaberrated telescope.

2.2 Speckle Holography Image Reconstruction

One modification to speckle interferometry, referred to as self-referenced speckle holography, was experimentally tested by the Air Force. During February of 1990 a combined Air Force and contractor team obtained images of stars using self-referenced speckle holography image reconstruction. The Air Force team was from the Air Force Phillips Laboratory and included John D. Gonglewski, D. G. Voelz, and J. S. Fender; the contractor team from Applied Technology Associates included D.C. Dayton, B.K. Spielbusch, and R.E. Pierson. The system (depicted in fig. 7) consisted of a 24 inch telescope, beam splitter, Shack-Hartmann wave front sensor array, and two CCD cameras (one for focal plane images and one for sensor spot images) (2:4527-4528). Prior to presenting the detailed experiment setup and results, the theory detailed by the report will be presented.

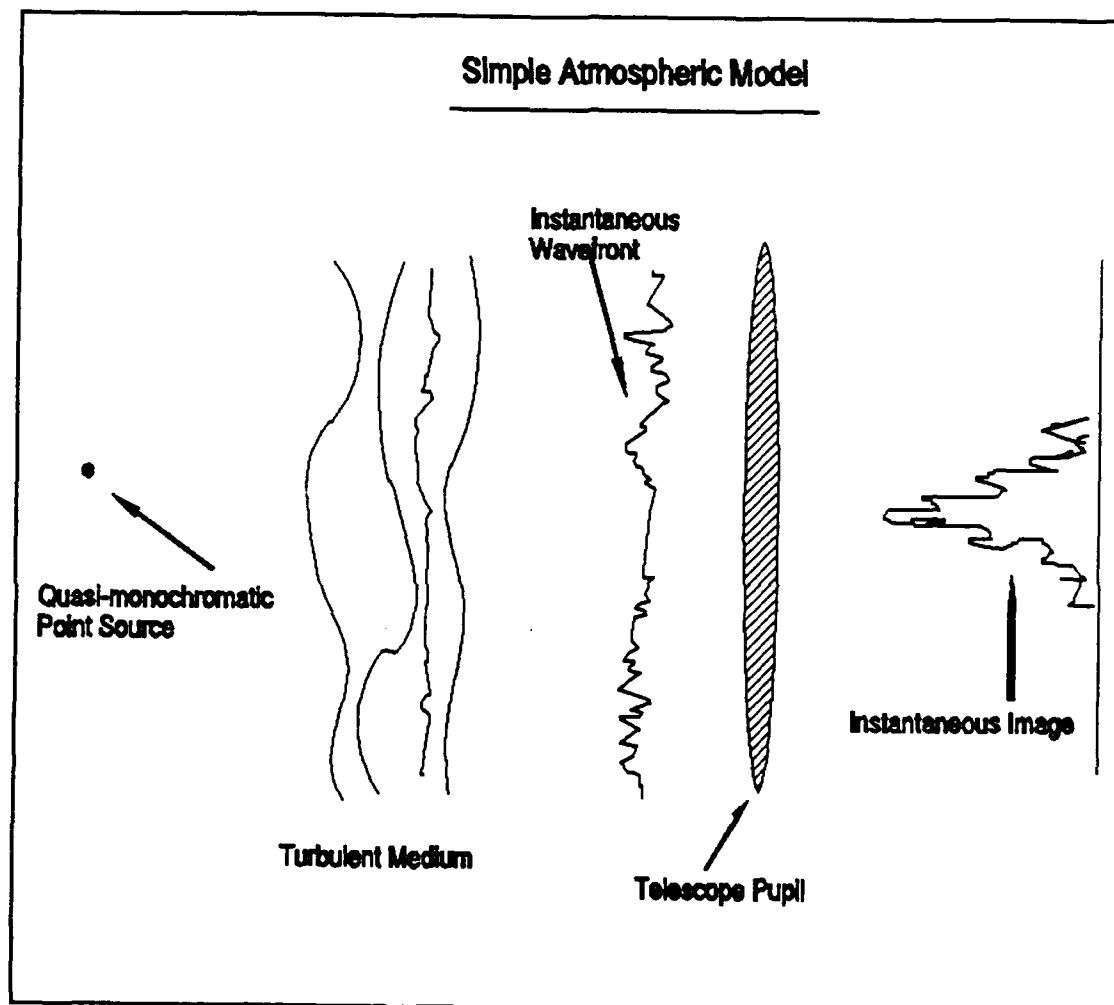


Fig. 5 Simplified atmospheric model of an instantaneous image through the atmosphere (5:260)

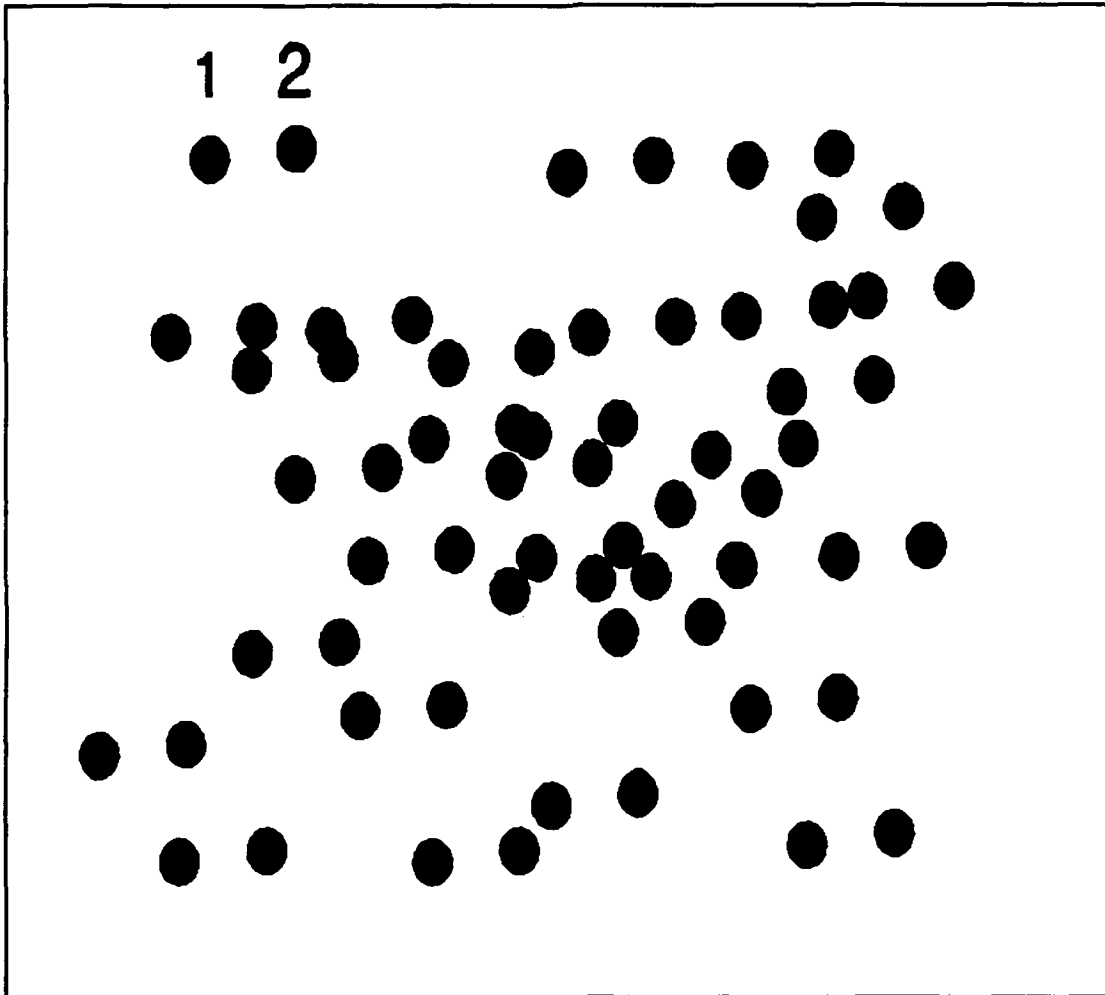


Fig. 6 Schematic diagram of the speckle pattern from a bright binary star whose components have equal magnitude; the black dots indicate bright speckles and are paired (5:268).

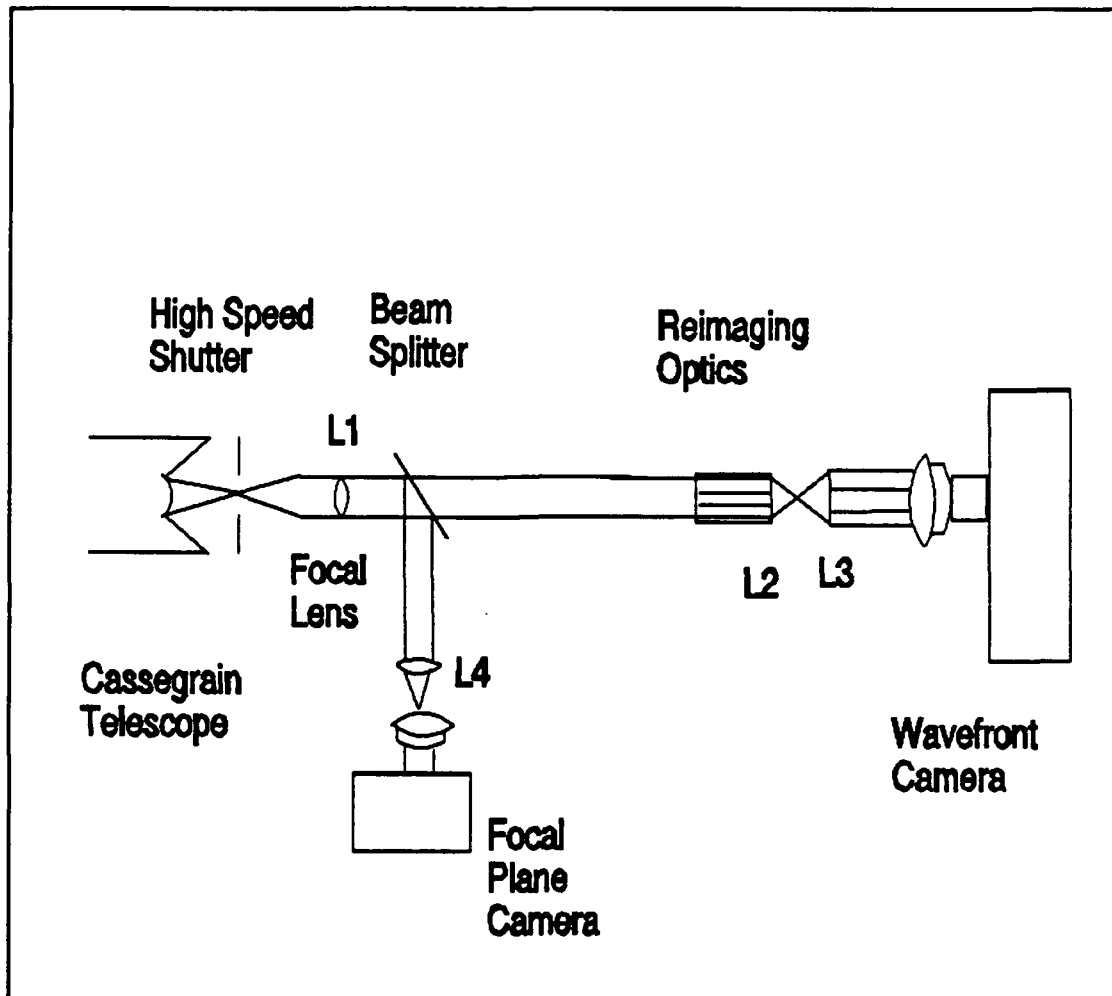


Fig. 7 Layout of self-referenced speckle holography instrument (2:4528).

2.2.1 **Theory of Self Referenced Speckle Holography:** As detailed in the experiment report, the atmospheric distortions act as a single layer phase screen. These phase distortions become localized tilts over the wave front. The Shack-Hartmann sensor measures these wave front tilts. The tilts from the wave front sensor are in turn used to obtain an estimate of the optical transfer function of the imaging system. To provide the mathematical theory this thesis turns to the explanation presented by the Phillips team.

For an imaging system it is well known that in the spatial domain that the image intensity distribution, $i(x,y)$, is related to the object intensity distribution, $o(x,y)$, convolved with the combined system and atmospheric point spread function, $h(x,y)$, where $*$ denotes convolution and x and y are transverse coordinates in the image plane (2:4527)

$$i(x,y) = o(x,y) * h(x,y) \quad (1)$$

Convolution in the spatial domain is equivalent to multiplication in the spatial frequency domain. Taking the Fourier transform of the image intensity distribution, the object intensity distribution and the point spread function the following relation results (2:4527)

$$I(u,v) = O(u,v) H(u,v) \quad (2)$$

where u and v are the spatial frequencies variables and are related to x and y as follows (f_d is the focal length of telescope)

$$u = \frac{x}{\lambda f_d} \quad (3)$$

$$v = \frac{y}{\lambda f_d} \quad (4)$$

As described by the Phillips team the function $\phi(u,v)$ describes the phase disturbance at the pupil of the imaging system and $P(u,v)$ is the pupil function. If $\phi(u,v)$ can be measured and $P(u,v)$ is known

then the optical transfer function is defined as

$$H(u, v) = P(u, v) \exp[2\pi j\phi(u, v)] \otimes P(u, v) \exp[2\pi j\phi(u, v)] \quad (5)$$

where \otimes denotes an autocorrelation. With $\phi(u, v)$ measured by the wave front sensor and $P(u, v)$ known the reconstruction algorithm becomes

$$O(u, v) = \frac{I(u, v) H^*(u, v)}{H(u, v) H^*(u, v) + \epsilon^2} \quad (6)$$

where the parametric constant ϵ^2 prevents the denominator from going to zero.

To obtain a better reconstruction, multiple image pairs can be used. in this case the algorithm becomes

$$O(u, v) = \frac{\langle I(u, v) H^*(u, v) \rangle}{\langle H(u, v) H^*(u, v) \rangle + \epsilon^2} \quad (7)$$

where $\langle \rangle$ denotes an ensemble average (2:4527).

2.2 Experiment Setup and Results: Referring again to figure 7, the optical wave front is passed through the Cassegrain telescope to a collimating lens (L1). To develop simultaneous records of the image intensity and the wave front tilt, the beam is split to provide photon energy to the wave front sensor and to the focal plane camera. The CCD cameras used for the image and wave front sensor records are low noise with 512 x 512 pixel segmentation. The wave front sensor consists of spherical lenslets of 100 μm diameter. The wave front is reimaged to span a 64 x 64 array of the lenslets. With a 512 x 512 pixel array for the wave front sensor each of the 64 x 64 subapertures spanned 8 x 8 pixels to record the spot focus.

With the tilt measurements a computer processing determines estimates of the optical transfer function and the point spread function. With digital deconvolution, an enhanced nearly diffraction limited reconstructed image is obtained (2:4528).

One of the three Phillips experimental results is provided. In this observation the exposure

time was 10 milliseconds, less than the correlation time of the atmosphere. The star observed was α Aurigae (Capella), of visual magnitude 0.08. Shown in the Phillips computer image figure 8A is the focal plane image with no correction. Figure 8B is the estimated point spread function obtained via the wave front sensor and computer analysis. Figure 8C is the image after deconvolution. As noted by the Phillips team the image has nearly diffraction limited resolution (2:4527). A spatial frequency spectrum analysis of this experiment is accomplished in Chapter IV.

2.3 Speckle Holography Image Reconstruction Analysis

In his article on "Deconvolution from Wave Front Sensing", J Primot presents the requirements for a system similar to the one used by the Phillips Laboratory in which they obtained the enhanced images. The major components of the system are a telescope, an imaging camera, and a wave front sensor conjugate with the entrance pupil of the image. If the images are obtained along with the sensor information (exposure requirements per frame are in the order of 1 to 10 milliseconds), the optical transfer function (OTF) can be assessed. Lost spatial frequencies in one frame will be available in subsequent frames, providing an essentially complete frequency spectrum (6:1598).

To better understand the methodology of the performance analysis in Section 3.3 it is important to follow Primot's reasoning. He begins with an object $o(x,y)$ imaged by a system through the atmosphere. The intensity of the short-exposure image at instant is $i(x,y)$. The point spread function of the atmosphere and telescope is $h(x,y)$. In the spatial domain, $i(x,y)$ is related to $o(x,y)$ by the convolution

$$i(x,y) = o(x,y) * h(x,y) \quad (8)$$

where $*$ denotes convolution. In the spatial frequency domain, taking Fourier transforms, the

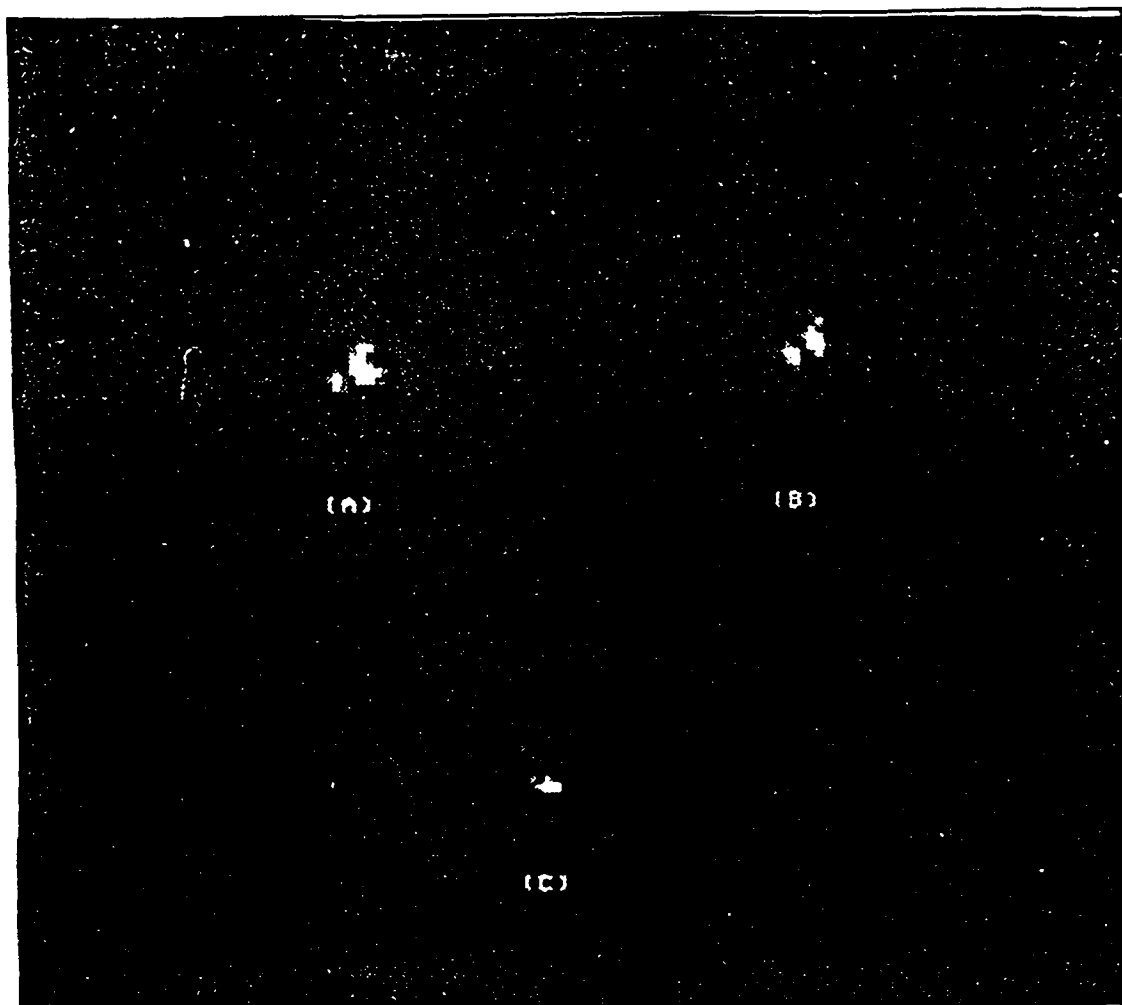


Fig. 8 Computer image of α Aurigae (Capella) image: (A) focal plane image; (B) atmospheric psf estimate; (C) compensated image (2:4528).

relationship becomes (6:1598)

$$I(u, v) = O(u, v) H(u, v) \quad (9)$$

where $H(u, v)$ is the instantaneous OTF. Theoretically if $H(u, v)$ is known then $O(u, v)$ can be computed as the ratio of $I(u, v)$ to $H(u, v)$. The instantaneous OTF can be zero in certain locations and as such the algorithm requires modification. Averaging the OTF over the records prevents the denominator from going to zero. The following relationship which will be expanded in Chapter III results (6:1598)

$$O(u, v) = \frac{\langle I(u, v) H(u, v)^* \rangle}{\langle H(u, v) H(u, v)^* \rangle} \quad (10)$$

To visualize Primot's processing algorithm, his flow diagram is shown in figure 9 (6:1599). Each short-exposure image $i(x, y)$ is Fourier transformed, and $H(u, v)$ is computed from the measured wave front. The average cross spectrum of the images and of the point spread functions and the average squared modulus of the OTF are then calculated over the records taken. Finally, the object is estimated by an inverse Fourier transform (6:1599).

2.4 System modelling

Papers written by Welsh (4:1913-1923) and Wallner (7:1771-1776) provide the baseline for the analysis. Discussion of these two papers is deferred until Chapter III.

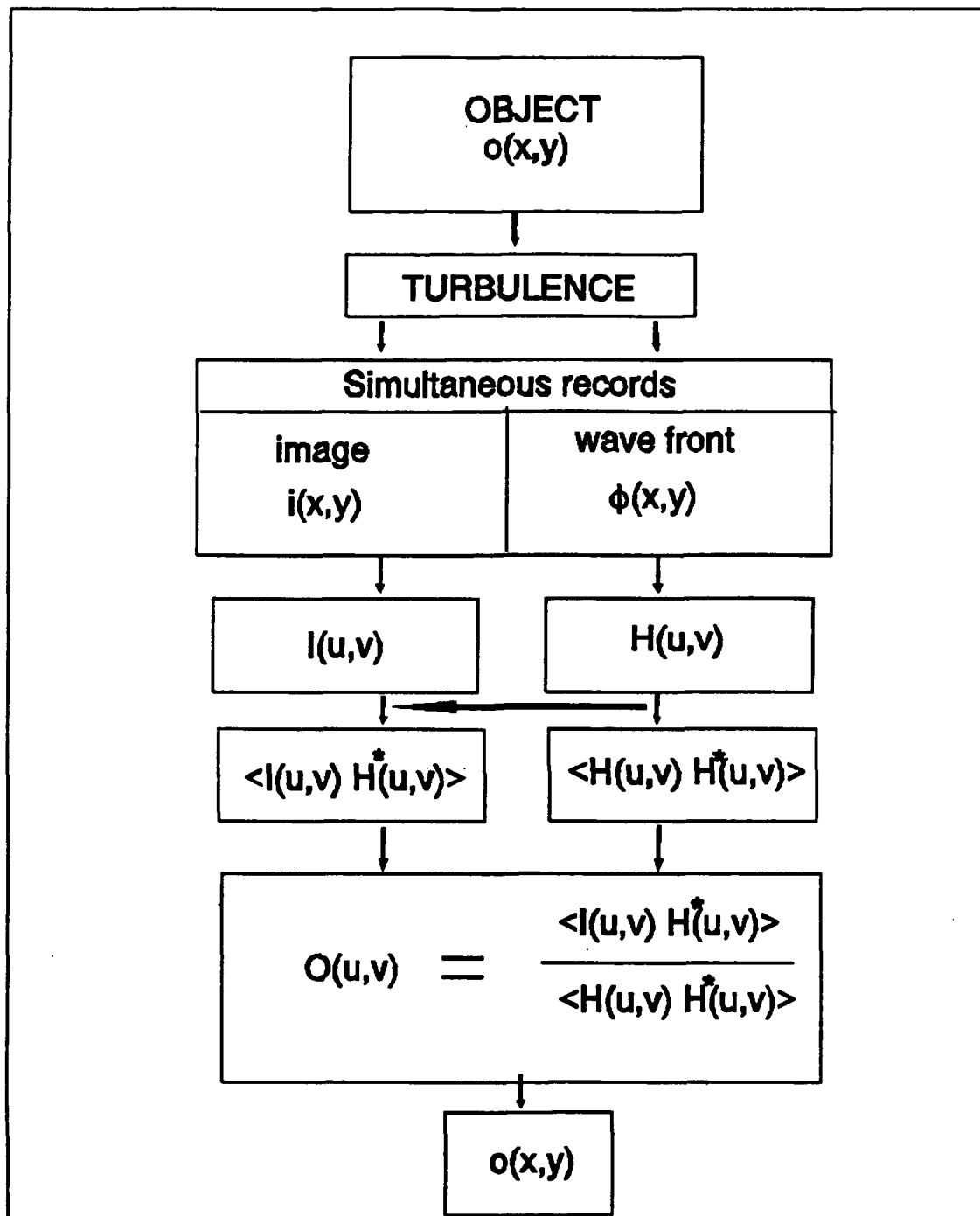


Fig. 9 Block diagram by J. Primot of the processing algorithm of the turbulence-degraded images to the object image restoration (6:1599).

III. Analysis

This chapter develops the analytic tools to evaluate two key system parameters for speckle holography image reconstruction. These two parameters are the ratio of the sensor subaperture size to the atmospheric coherence diameter r_0 , L/r_0 , and the number of photons incident on the subaperture, N . A system transfer function (STF) which includes the transfer function of the telescope combined with the transfer function of the atmosphere and the computer processing algorithms is developed. The development begins with key system models developed by Wallner and Welsh and culminates in the development of the system transfer function algorithm from the background theory provided in Chapter II.

3.1 System Models

The following model descriptions closely follow those of Wallner (7:1771-1776), and Welsh and Gardner (4:1913-1923). These brief descriptions are included here to show explicitly how the factors that degrade imaging performance and impact the system transfer function are incorporated into the results. The following model descriptions are very general and are applicable to a wide range of atmospheric compensation systems. For the performance analysis of this thesis, the system transfer function algorithm is based on a system consisting of a wave front sensor (WFS), aperture, and a wave front reconstructor. The wave front reconstructor is based on an array of Gaussian interpolation functions. Figure 10 illustrates the corresponding sensor coverage of a square aperture plane by a 5×5 sensor array. The dots correspond to the centers of the Gaussian interpolation functions used in the wave front reconstructor. The wave front sensor and the square pupil plane are optically conjugated. The wave front sensor senses the gradient of the distorted phase. The pupil is segmented into a finite number of subapertures and the wave front sensor measures the average phase slope or tilt of the referenced wave front within each subaperture. This thesis concentrated on phase

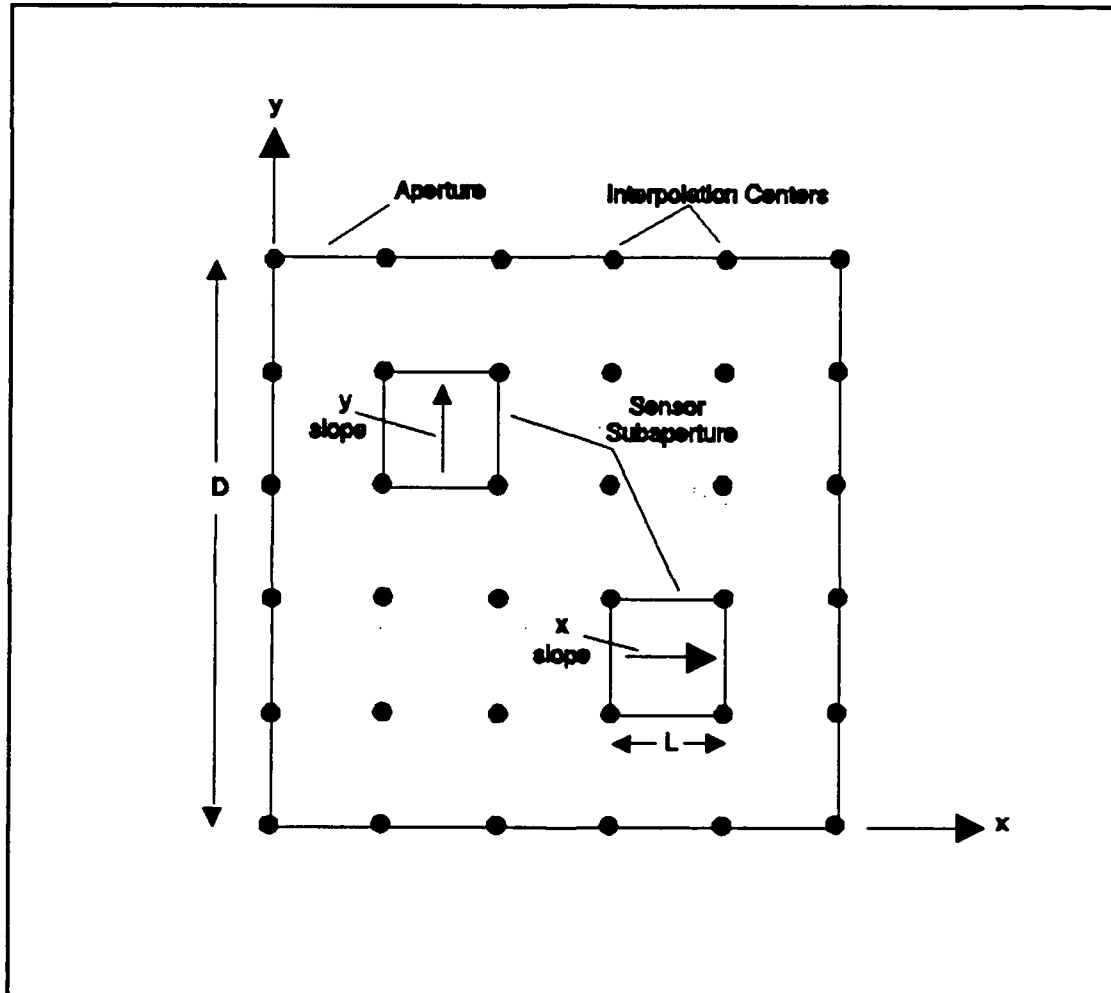


Fig. 10 Conjugate aperture and wave front sensor planes (7:1775).

correction and assumed that turbulence induced amplitude effects are negligible.

The pupil of the optical system is described by the weighting function $W_A(\mathbf{x})$ (m^2) where $\mathbf{x}(\text{m})$ is a 2 dimensional vector in the pupil plane. It is convenient to normalize $W_A(\mathbf{x})$ such that

$$\int_{-\infty}^{\infty} d^2\mathbf{x} W_A(\mathbf{x}) = 1 \quad (11)$$

For the results presented in this thesis $W_A(\mathbf{x})$ describes a square aperture.

The wave front sensor senses the phase perturbations of the wave front. The phase perturbations of the point source is designated as $\psi(\mathbf{x})$. $\psi(\mathbf{x})$ is treated as a gaussian random process in space. To facilitate the analysis it is convenient to define a zero-mean phase $\phi(\mathbf{x})$ which is related to $\psi(\mathbf{x})$ by (4:1914)

$$\phi(\mathbf{x}) = \psi(\mathbf{x}) - \int d^2\mathbf{x}' W_A(\mathbf{x}') \psi(\mathbf{x}') \quad (12)$$

The output of the n th sensor in the WFS is a noisy measurement of the average slope of $\phi(\mathbf{x})$ over the n th subaperture $W_n(\mathbf{x})$

$$s_n = \int d^2\mathbf{x} W_n(\mathbf{x}) [\nabla\phi_n(\mathbf{x}) \cdot \hat{\mathbf{d}}_n] + \alpha_n \quad (13)$$

where

s_n is the signal from the n th sensor,

$W_n(\mathbf{x})$ is the weighting function for the n th sensor,

$\nabla\phi_n(\mathbf{x})$ is the slope of the wave front in the direction of sensitivity of the n th sensor,

$\hat{\mathbf{d}}_n$ is a unit vector in the direction of sensitivity of the n th

α_n is the slope measurement error for the n th sensor.

The subaperture weighting function $W_n(\mathbf{x})$ is defined in a manner similar to the $W_A(\mathbf{x})$ in eqn (11).

The slope measurement noise α_n is due to shot noise effects and is assumed random having a

Gaussian distribution with zero mean and a variance σ_n^2 .

The wave front reconstructor generates a weight for each Gaussian interpolation function based on the slope measurements. Using a linear reconstructor the j th weight is defined by c_j (7:1772)

$$c_j = \sum M_{jn} s_n \quad (14)$$

M_{jn} is the weighting of the n th sensor signal in the j th interpolation function weight.

Finally the reconstructed object wave front phase $\hat{\phi}$ is defined as

$$\hat{\phi}(\mathbf{x}) = \sum c_j r_j(\mathbf{x}) \quad (15)$$

where $r_j(\mathbf{x})$ is the response of the j th interpolation function to a unit weight.

With the model descriptions outlined in eqns (11) through (15) the purpose of this section is to derive the optimal M_{jn} reconstructor matrix. The optimal M_{jn} reconstructor matrix is derived by minimizing the mean-square phase error. The mean-square phase error between the actual phase and the reconstructed phase over the corrected telescope pupil is

$$\langle \epsilon^2(\mathbf{x}) \rangle = \langle [\hat{\phi}(\mathbf{x}) - \phi(\mathbf{x})]^2 \rangle \quad (16)$$

where the operator $\langle \rangle$ designates an ensemble average. Averaging $\langle \epsilon^2(\mathbf{x}) \rangle$ over the telescope gives

$$\langle \epsilon^2 \rangle = \int d^2(\mathbf{x}) W_A(\mathbf{x}) \langle \epsilon^2(\mathbf{x}) \rangle \quad (17a)$$

$$= \int d^2(\mathbf{x}) W_A(\mathbf{x}) \langle [\hat{\phi}(\mathbf{x}) - \phi(\mathbf{x})]^2 \rangle \quad (17b)$$

Wallner shows that $\langle \epsilon^2 \rangle$ can be minimized with the optimum choice of the M_{jn} matrix. The optimum matrix M_{jn}^* is given by (7:1773)

$$M_{jn}^* = \sum_{j'} \sum_{n'} R_{jj'}^{-1} A_{j'/n'} S_{n'n}^{-1} \quad (18)$$

where R, A and S are matrices that depend on the specific characteristics of the WFS, wave front reconstructor, and the statistics of the phase fluctuations. The jj' 'th element of R is the correlation of the j 'th and j' 'th influence functions. The nn' 'th element of S is the correlation of the n 'th and n' 'th slope measurements. Finally, the $j'n'$ 'th element of A describes the correlation of the j' 'th interpolation function with the n' 'th slope measurement. Expressions for R, A, and S are given by Welsh and Gardner.

3.2 System Transfer Function Algorithm Development

With the system models in hand this thesis will develop the system transfer function. From the baseline theory in Chapter II eqn (10), the spatial frequency domain estimate of $\hat{O}(\rho)$ is

$$\hat{O}(\rho) = \frac{\langle I(\rho) \hat{H}^*(\rho) \rangle}{\langle \hat{H}(\rho) \hat{H}^*(\rho) \rangle} \quad (19)$$

where

$$\rho = u\hat{x} + v\hat{y} \quad (20)$$

In normal systems the transfer function is derived from the input of a delta function. For this thesis the delta function in the spatial domain will be a star. The star is essentially a point source

in intensity distribution. With the object defined as a point source i.e. $\delta(x,y)$, the following results

$$i(x,y) = \delta(x,y) * h(x,y) = h(x,y) \quad (21)$$

After Fourier transforming

$$I(\rho) = H(\rho) \quad (22)$$

Substituting eqn (22) into eqn (19) the STF becomes

$$\hat{O}(\rho) = \frac{\langle H(\rho) \hat{H}^*(\rho) \rangle}{\langle \hat{H}(\rho) \hat{H}^*(\rho) \rangle} \quad (23)$$

$H(\rho)$ is the optical transfer function of the combined atmosphere and telescope and is defined as follows

$$H(\rho) = \int d^2x W_A(x) W_A(x-\rho) \exp[j\phi(x)] \exp[-j\phi(x-\rho)] \quad (24)$$

The estimate of the optical transfer function is defined by

$$\hat{H}(\rho) = \int d^2x W_A(x) W_A(x-\rho) \exp[j\hat{\phi}(x)] \exp[-j\hat{\phi}(x-\rho)] \quad (25)$$

Substituting eqn (24) and eqn (25) into eqn (23) results in

$$\hat{O}(\rho) = \frac{\int d^2x \int d^2x' W_A(x) W_A(x') W_A(x-\rho) W_A(x'-\rho)}{\int d^2x \int d^2x' W_A(x) W_A(x') W_A(x-\rho) W_A(x'-\rho)} \quad (26)$$

$$\times \frac{\langle \exp[j\phi(x) - j\hat{\phi}(x) - j\phi(x-\rho) + j\hat{\phi}(x-\rho)] \rangle}{\langle \exp[j\hat{\phi}(x) - j\hat{\phi}(x) - j\hat{\phi}(x-\rho) + j\hat{\phi}(x-\rho)] \rangle}$$

Using the fact that $\phi(x)$ and $\hat{\phi}(x)$ are assumed to have Gaussian statistics (8:20), it is possible to write eqn (26) as moments such that

$$\hat{O}(\rho) = \frac{\int d^2x \int d^2x' W_A(x) W_A(x') W_A(x-\rho) W_A(x'-\rho)}{\int d^2x \int d^2x' W_A(x) W_A(x') W_A(x-\rho) W_A(x'-\rho)} \quad (27)$$

$$\frac{\exp\left[-\frac{1}{2} \langle [\phi(x) - \hat{\phi}(x') - \phi(x-\rho) + \hat{\phi}(x'-\rho)]^2 \rangle\right]}{\exp\left[-\frac{1}{2} \langle [\hat{\phi}(x) - \hat{\phi}(x') - \hat{\phi}(x-\rho) + \hat{\phi}(x'-\rho)]^2 \rangle\right]}$$

The second order statistical characteristics of $\phi(x)$ are defined in terms of the phase structure function

$$D(x, x') = \langle [\psi(x) - \psi(x')]^2 \rangle \quad (28)$$

Carrying out the squaring in eqn (27) will result in variations of Wallner's phase correlation $\langle \phi(x) \phi(x') \rangle$, his phase correlation is defined as follows (7:1773)

$$\langle \phi(x) \phi(x') \rangle = -1/2 D(x, x') + g(x) + g(x') - a \quad (29)$$

where,

$$a = \frac{1}{2} \int dx'' \int dx''' W_A(x'') W_A(x''') D(x'', x''') \quad (30)$$

and

$$g(x) = \frac{1}{2} \int dx'' W_A(x'') D(x, x'') \quad (31)$$

With the correlation of $\langle \phi(x)\phi(x') \rangle$ defined it is possible to continue with the STF development. For ease in understanding the STF is segmented into the numerator

$$STF_{numerator}(\rho) = \int d^2x \int d^2x' W_A(x) W_A(x') W_A(x-\rho) W_A(x'-\rho) \quad (32)$$

$$x \{ \exp[(-\frac{1}{2}) \langle [\phi(x) - \phi(x') - \phi(x-\rho) + \phi(x'-\rho)]^2 \rangle] \}$$

and the denominator

$$STF_{denominator}(\rho) = \int d^2x \int d^2x' W_A(x) W_A(x') W_A(x-\rho) W_A(x'-\rho) \quad (33)$$

$$x \{ \exp[(-\frac{1}{2}) \langle [\phi(x) - \phi(x') - \phi(x-\rho) + \phi(x'-\rho)]^2 \rangle] \}$$

After squaring eqn (32) and eqn (33) there are 16 terms for both the numerator and the denominator. Using the phase correlation relationship developed by Wallner (7:1773) a correlation equivalence is presented for each of the terms. The correlation of the phase terms $\langle \phi(\mathbf{x})\phi(\mathbf{x}') \rangle$ and its corresponding relationship as derived from eqn (29) is presented. The terms of the STFnumerator are presented in Table I and the terms of the STFdenominator are presented in Table II.

Table I. STFnumerator Correlation Equivalence

Term =	CorrelationEquivalence
$\langle \phi(x)\phi(x) \rangle =$	$2g(x) - a$
$-\langle \hat{\phi}(x)\hat{\phi}(x') \rangle =$	$-(1/2)\sum_j \sum_n r_j(x') \int d^2x'' W_n^*(x'') [D(x, x'') - 2g(x'')]]$
$-\langle \phi(x)\phi(x-\rho) \rangle =$	$(1/2)[D(x, x-\rho) - 2g(x) - 2g(x-\rho) + 2a]$
$\langle \phi(x)\hat{\phi}(x'-\rho) \rangle =$	$(1/2)\sum_j \sum_n M_{jn} r_j(x'-\rho) \int d^2x'' W_n^*(x'') [D(x, x'') - 2g(x'')]]$
$-\langle \hat{\phi}(x)\hat{\phi}(x') \rangle =$	$-(1/2)\sum_j \sum_n r_j(x') \int d^2x'' W_n^*(x'') [D(x, x'') - 2g(x'')]]$
$\langle \hat{\phi}(x')\hat{\phi}(x') \rangle =$	$\sum_i \sum_j c_{ij} r_i(x') r_j(x')$
$\langle \phi(x-\rho)\hat{\phi}(x') \rangle =$	$(1/2)\sum_j \sum_n M_{jn} r_j(x') \int d^2x'' W_n^*(x'') [D(x-\rho, x'') - 2g(x'')]]$
$-\langle \hat{\phi}(x')\hat{\phi}(x'-\rho) \rangle =$	$-\sum_i \sum_j c_{ij} r_i(x') r_j(x'-\rho)$
$-\langle \phi(x)\phi(x-\rho) \rangle =$	$(1/2)[D(x, x-\rho) - 2g(x) - 2g(x-\rho) + 2a]$
$\langle \phi(x-\rho)\hat{\phi}(x') \rangle =$	$(1/2)\sum_j \sum_n M_{jn} r_j(x') \int d^2x'' W_n^*(x'') [D(x-\rho, x'') - 2g(x'')]]$
$\langle \phi(x-\rho)\phi(x-\rho) \rangle =$	$2g(x-\rho) - a$
$-\langle \hat{\phi}(x-\rho)\hat{\phi}(x'-\rho) \rangle =$	$-(1/2)\sum_j \sum_n M_{jn} r_j(x'-\rho) \int d^2x'' W_n^*(x'') [D(x-\rho, x'') - 2g(x'')]]$
$\langle \phi(x)\hat{\phi}(x'-\rho) \rangle =$	$(1/2)\sum_j \sum_n M_{jn} r_j(x'-\rho) \int d^2x'' W_n^*(x'') [D(x, x'') - 2g(x'')]]$
$-\langle \hat{\phi}(x'-\rho)\hat{\phi}(x') \rangle =$	$-\sum_i \sum_j c_{ij} r_i(x'-\rho) r_j(x')$
$-\langle \hat{\phi}(x-\rho)\hat{\phi}(x'-\rho) \rangle =$	$-(1/2)\sum_j \sum_n M_{jn} r_j(x'-\rho) \int d^2x'' W_n^*(x'') [D(x-\rho, x'') - 2g(x'')]]$
$\langle \hat{\phi}(x'-\rho)\hat{\phi}(x'-\rho) \rangle =$	$\sum_i \sum_j c_{ij} r_i(x'-\rho) r_j(x'-\rho)$

where

$$C_{ij} = \langle c_i c_j \rangle = \sum_n \sum_m M_{jn} M_{in} S_{nm}$$

Table II. STFdenominator Correlation Equivalence

Term	CorrelationEquivalence
$\langle \hat{\phi}(x)\hat{\phi}(x) \rangle =$	$\sum_i \sum_j C_{ij} r_i(x) r_j(x)$
$-\langle \hat{\phi}(x)\hat{\phi}(x') \rangle =$	$-\sum_i \sum_j c_{ij} r_i(x) r_j(x')$
$-\langle \hat{\phi}(x)\hat{\phi}(x-\rho) \rangle =$	$-\sum_i \sum_j c_{ij} r_i(x) r_j(x-\rho)$
$\langle \hat{\phi}(x)\hat{\phi}(x'-\rho) \rangle =$	$\sum_i \sum_j c_{ij} r_i(x) r_j(x'-\rho)$
$-\langle \hat{\phi}(x')\hat{\phi}(x) \rangle =$	$-\sum_i \sum_j c_{ij} r_i(x') r_j(x)$
$\langle \hat{\phi}(x')\hat{\phi}(x') \rangle =$	$\sum_i \sum_j c_{ij} r_i(x') r_j(x')$
$\langle \hat{\phi}(x')\hat{\phi}(x-\rho) \rangle =$	$\sum_i \sum_j c_{ij} r_i(x') r_j(x-\rho)$
$-\langle \hat{\phi}(x')\hat{\phi}(x'-\rho) \rangle =$	$-\sum_i \sum_j c_{ij} r_i(x') r_j(x'-\rho)$
$-\langle \hat{\phi}(x-\rho)\hat{\phi}(x) \rangle =$	$-\sum_i \sum_j c_{ij} r_i(x-\rho) r_j(x)$
$\langle \hat{\phi}(x-\rho)\hat{\phi}(x') \rangle =$	$\sum_i \sum_j c_{ij} r_i(x-\rho) r_j(x')$
$\langle \hat{\phi}(x-\rho)\hat{\phi}(x-\rho) \rangle =$	$\sum_i \sum_j c_{ij} r_i(x-\rho) r_j(x-\rho)$
$-\langle \hat{\phi}(x-\rho)\hat{\phi}(x'-\rho) \rangle =$	$-\sum_i \sum_j c_{ij} r_i(x-\rho) r_j(x'-\rho)$
$\langle \hat{\phi}(x'-\rho)\hat{\phi}(x) \rangle =$	$\sum_i \sum_j c_{ij} r_i(x'-\rho) r_j(x)$
$-\langle \hat{\phi}(x'-\rho)\hat{\phi}(x') \rangle =$	$-\sum_i \sum_j c_{ij} r_i(x'-\rho) r_j(x')$
$-\langle \hat{\phi}(x'-\rho)\hat{\phi}(x-\rho) \rangle =$	$-\sum_i \sum_j c_{ij} r_i(x'-\rho) r_j(x-\rho)$
$\langle \hat{\phi}(x'-\rho)\hat{\phi}(x'-\rho) \rangle =$	$\sum_i \sum_j c_{ij} r_i(x'-\rho) r_j(x'-\rho)$

With the mathematical manipulation of the terms, several terms cancel out and several terms combine in the numerator resulting in

$$STF_{numerator}(\rho) = \exp \frac{-D(\mathbf{x}, \mathbf{x} - \rho)}{2} \times \left\{ \int d^2\mathbf{x} \int d^2\tilde{\mathbf{x}} W_A(\mathbf{x}) W_A(\tilde{\mathbf{x}}) W_A(\mathbf{x} - \rho) W_A(\tilde{\mathbf{x}} - \rho) \right\} \quad (34)$$

$$\times \exp \left\{ -\frac{1}{2} \sum_i \sum_j C_{ij} [r_i(\tilde{\mathbf{x}}) - r_i(\tilde{\mathbf{x}} - \rho)] [r_j(\tilde{\mathbf{x}}) - r_j(\tilde{\mathbf{x}} - \rho)] \right\}$$

$$\times \exp \left\{ \frac{1}{2} \sum_j [r_j(\tilde{\mathbf{x}}) - r_j(\tilde{\mathbf{x}} - \rho)] \sum_n M_{jn} \int d^2\tilde{\mathbf{x}} W_n(\tilde{\mathbf{x}}) [D(\mathbf{x}, \tilde{\mathbf{x}}) - D(\mathbf{x} - \rho, \tilde{\mathbf{x}})] \right\}$$

Similar manipulation of the terms results in the STF denominator

$$STF_{denominator}(\rho) = \int d^2\mathbf{x} \int d^2\tilde{\mathbf{x}} W_A(\mathbf{x}) W_A(\tilde{\mathbf{x}}) W_A(\mathbf{x} - \rho) W_A(\tilde{\mathbf{x}} - \rho) \exp \left\{ -\frac{1}{2} \sum_i \sum_j C_{ij} \{ [r_i(\mathbf{x}) - r_i(\mathbf{x} - \rho)] - [r_i(\tilde{\mathbf{x}}) - r_i(\tilde{\mathbf{x}} - \rho)] \} \right\} \quad (35)$$

$$\times \{ [r_j(\mathbf{x}) - r_j(\mathbf{x} - \rho)] - [r_j(\tilde{\mathbf{x}}) - r_j(\tilde{\mathbf{x}} - \rho)] \}$$

3.3 STF Numerical Analysis

With the system transfer algorithm defined and the aperture and wave front sensor models described this thesis will present the numerical results in Chapter IV.

IV. Results

This chapter provides the results of numerical evaluation of the system transfer function (STF). The software was derived from software developed by Welsh for his optical transfer function analysis (4:1913-1923). The analytical results of Chapter III were evaluated both on a VAX 11/785 at the Air Force Institute of Technology and a CRAY Y-MP8/864 supercomputer at Ohio State University, Columbus Ohio.

Prior to presenting the numerical results, a presentation of the slope measurement noise, the wave front reconstructor interpolation function, the phase-structure function, and the aperture and the wave front sensor geometry is provided. Also a pictorial representation of an ideal system is provided along with a representative of the results obtained is shown. Following the representative results, the three system parameters, number of subapertures across one row of the aperture, L/r_0 ratio (subaperture ratio to the atmospheric coherence diameter r_0), and N , photon count (total photons incident on a subaperture) were varied and the results provided. The definition and results will be provided for the system spread function and the system Strehl ratio. Because of the inclusion of the wave front reconstructor into the system transfer function analysis, the system spread function and the system Strehl ratio are characterized by the overall system. Finally, the parameters used by the Air Force Phillips laboratory for their experiment is analyzed to provide the frequency response of their experiment for the imaging of the α Aurigae.

4.1 Slope Measurement Noise

The following description of slope measurement noise closely follows that of Wallner (7:1773), and Welsh and Gardner (4:1917). The slope measurement noise is modeled with a random, zero-mean, slope signal α_n . This error signal is attributed to photon noise in the slope detection process. The slope measurement noise on nonoverlapping subapertures and on orthogonal

measurements on coincident subapertures are uncorrelated. These characteristics result in the correlation function (7:1774)

$$\langle \alpha_n \alpha_{n'} \rangle = \sigma_\alpha^2 k_{nn'} \delta_{nn'} \quad (36)$$

where

σ_α^2 is the ms slope error (in square radians per square meter),

$k_{nn'}$ is $\mathbf{1}_n \cdot \mathbf{1}_{n'}$ for n and n' measured simultaneously on the same area of the same wave front and is 0 otherwise

$\mathbf{1}_n$ is a unit vector in the direction of slope sensitivity of the n th measurement, and

$\delta_{nn'}$ is 1 when $n = n'$ and 0 otherwise

The magnitude of σ_α^2 depends on the wave front sensor. In this thesis the Hartmann sensor is used (4:1917).

The model of the wave front sensor was treated by Wallner (7:1774), and Welsh and Gardner (4:1918). In each subaperture the slope is sensed in both the x and y direction (see fig. 11). Extensive derivation by Kane (9:160-171) is performed to obtain the slope measurement accuracy σ_α and only the results are included for completeness. The resulting slope measurement accuracy is (4:1919)

$$\begin{aligned} \sigma_\alpha &= \frac{0.86\pi\eta}{N^{1/2}r_o} & L > r_o \\ \sigma_\alpha &= \frac{0.74\pi\eta}{N^{1/2}L} & L \leq r_o \end{aligned} \quad (37)$$

where $\eta = 1.5$ a value typical for currently charge coupled device detector arrays (4:1919).

4.2 Wave Front Reconstructor

The wave front reconstructor is a Gaussian interpolation function defined by

$$r_j(x, y) \propto \exp \left[\frac{-(x-x_j)^2 - (y-y_j)^2}{L_a^2} \right] \quad (38)$$

where x and y specify a point in the plane of the reconstructor and L_a is the influence radius (4:1917).

4.3 Phase-Structure Function

If the assumption is made that the turbulence layers are confined to a relatively narrow vertical region in the atmosphere, and that the turbulence is described by Kolmogorov statistics, then the approximation derived by Fried (10:1372-1379) can be used for the phase-structure function with

$$D(x, x') = 6.8839 \left(\frac{|x - x'|}{r_0} \right)^{\frac{5}{3}} \quad (39)$$

4.4 Aperture, Wave Front Sensor and Reconstructor Description

Before presenting the results a description of the aperture, the wave front sensor, and the wave front reconstructor is in order. The aperture is square and is optically conjugated with the wave front sensor and the wave front reconstructor. The description of the wave front sensor used was presented by Wallner (7:1774). The wave front sensor is a Hartmann sensor. The slope is measured in each subaperture in both the x and y directions. Figure 11 illustrates the optically conjugate aperture, wave front sensor, and the wave front reconstructor. The dots are the centers of the Gaussian interpolation functions used for the reconstruction of the phase. The square aperture has dimension D with subapertures of length L . Slope is measured by x and y sensors as shown. The system shown in figure 11 is a 5×5 sensor configuration.

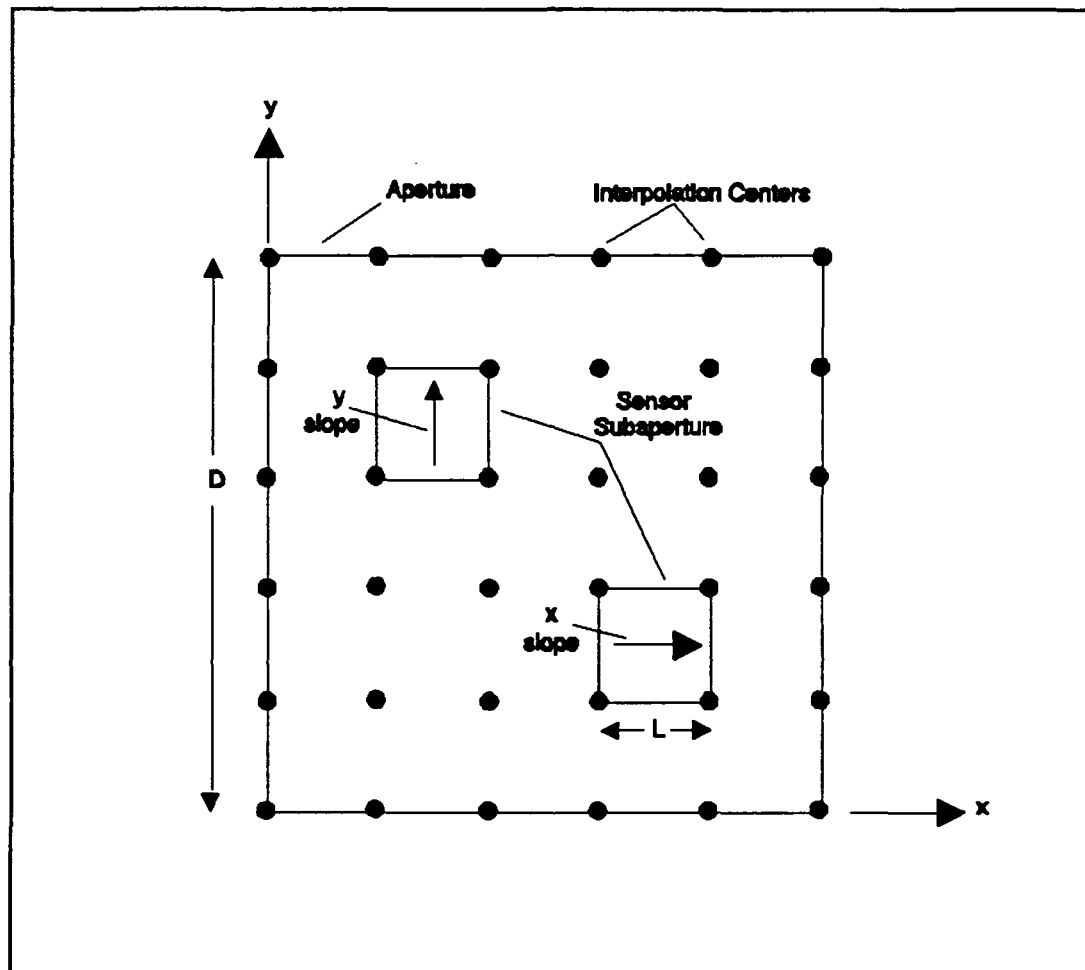


Fig. 11 Conjugate square aperture, wave front sensor and wave front reconstructor (7:1775).

4.5 *Idealized Numerical Results*

The pictorial representation of an ideal system transfer function response is provided in figure 12. In the ideal condition the wave front does not pass through the random phase screen of the turbulent atmosphere. In this case the optical transfer function is limited only to the diffraction limit of the telescope and resembles a triangle function for a square telescope aperture if the negative spatial frequencies are included. This is the unaberrated optical transfer function described by Goodman (8:378). Eqn (29) is represented pictorially in figure 12. With the optical transfer function and estimates of the optical transfer functions the system transfer function will be a rectangle function over the normalized spatial frequency.

4.6 *Expected results*

In the real world the phase screen of the turbulent atmosphere must be considered. The overall optical transfer function of the imaging system includes the transfer function of the turbulent atmosphere. On decreasing the size of the sensor subaperture and increasing photon count per subaperture the STF approaches a rectangle function. As the sensor subaperture size is decreased, greater precision in the measurement of the wave front tilt results. Boosting of the higher spatial frequencies is tied to the subaperture size as will be shown later. The representative case of the numerical results obtained for this thesis is depicted in figure 13.

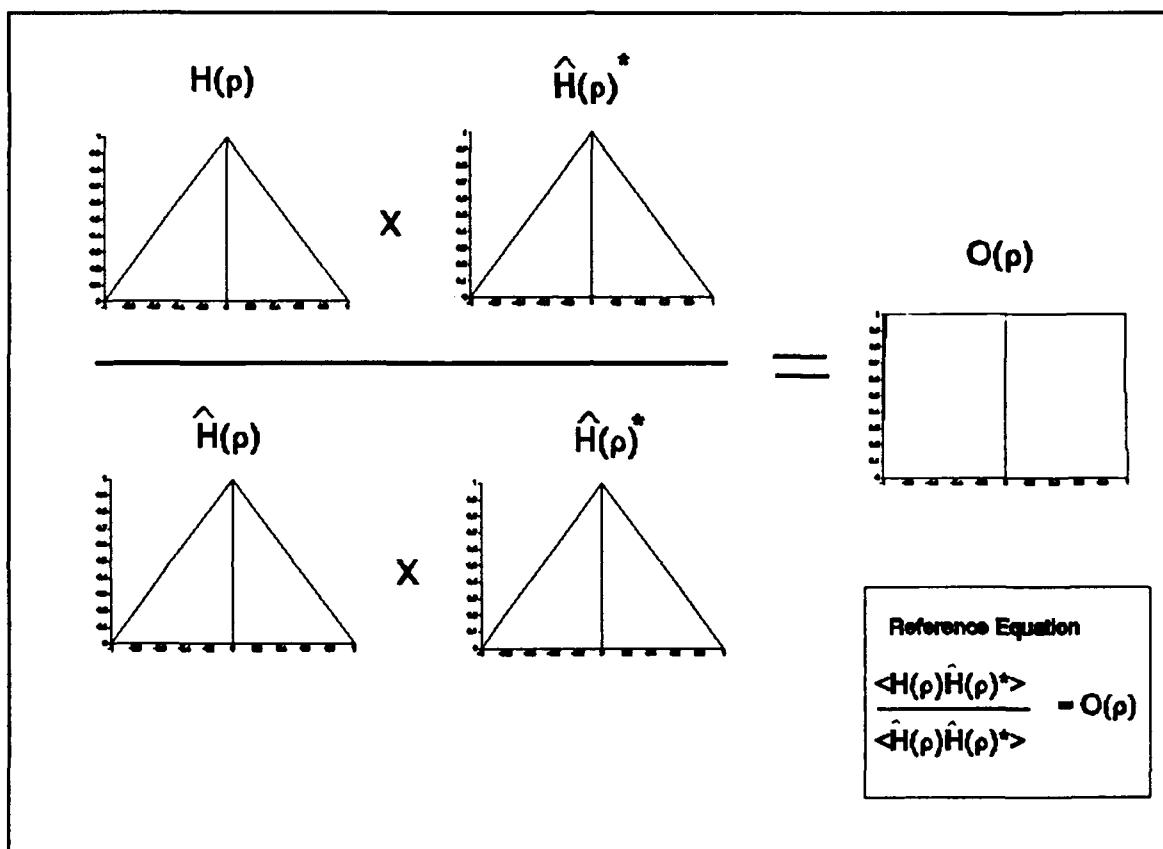


Fig. 12 System transfer function results for ideal case.

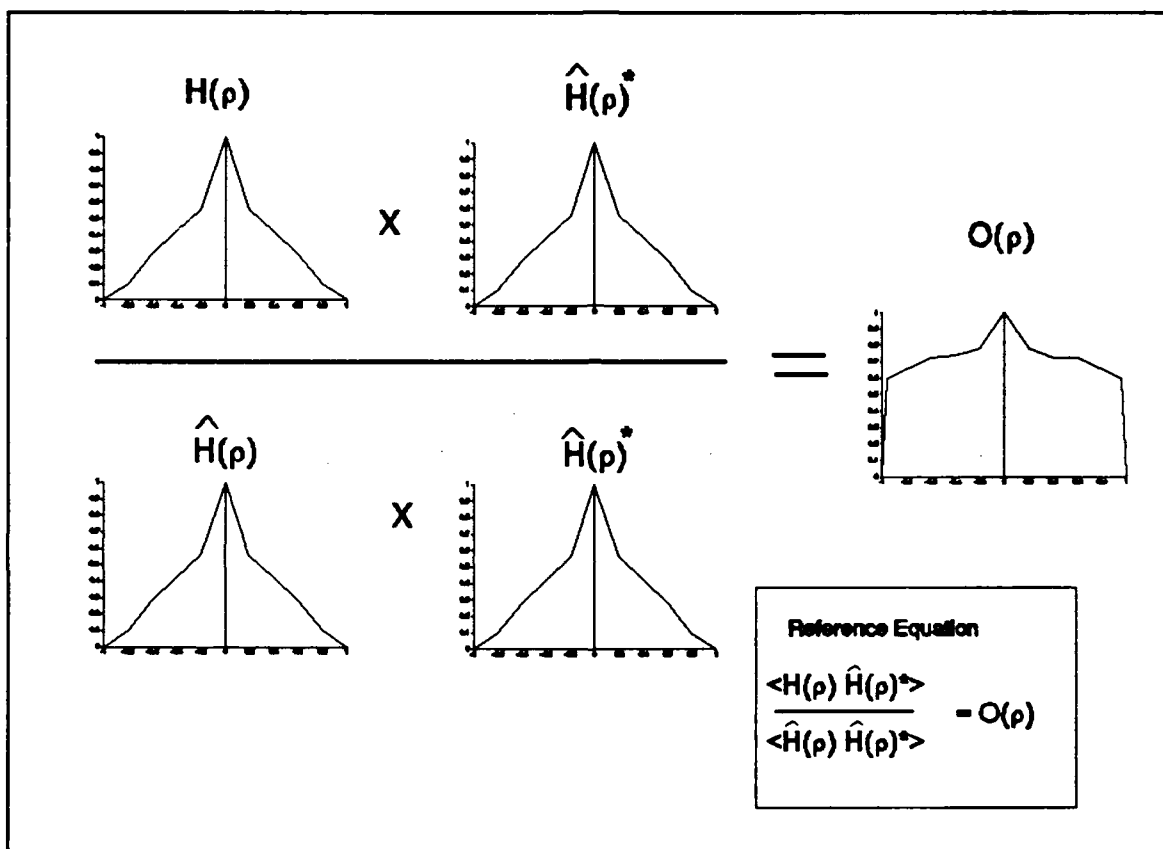


Fig. 13 System transfer function results for a representative case.

4.7 Variation in Photon Count

The results presented are similar in nature to the way Welsh presented results for the optical transfer function (4:1921). The first results presented are changes in photon count on the subaperture. The sensor configuration consists of both a 2 x 2 and a 5 x 5 wave front sensor. The results for the 2 x 2 were obtained on the VAX 11/785, while the results of the 5 x 5 were obtained on the Cray. The results of the computations are presented as plots of magnitude of the STF versus ρ/D where the spatial frequency u is related to ρ by $u = \rho/\lambda f_D$, and f_D is the focal length of the aperture lens. The vector ρ is limited to the x direction (4:1921).

The line on each plot marked ideal is the plot of the ideal system transfer function discussed in 4.1. The number of photons per subaperture N is annotated. The graph depicts the dependence on photon incidence. The greater the photon incidence per subaperture the higher the STF magnitude. An additional six figures are provided representing the dependence on photon incidence. Figures 15-17 increases the subaperture size to atmospheric coherence diameter ratio (L/r_o ratio), while figures 18-20 address 5 x 5 subaperture configuration.

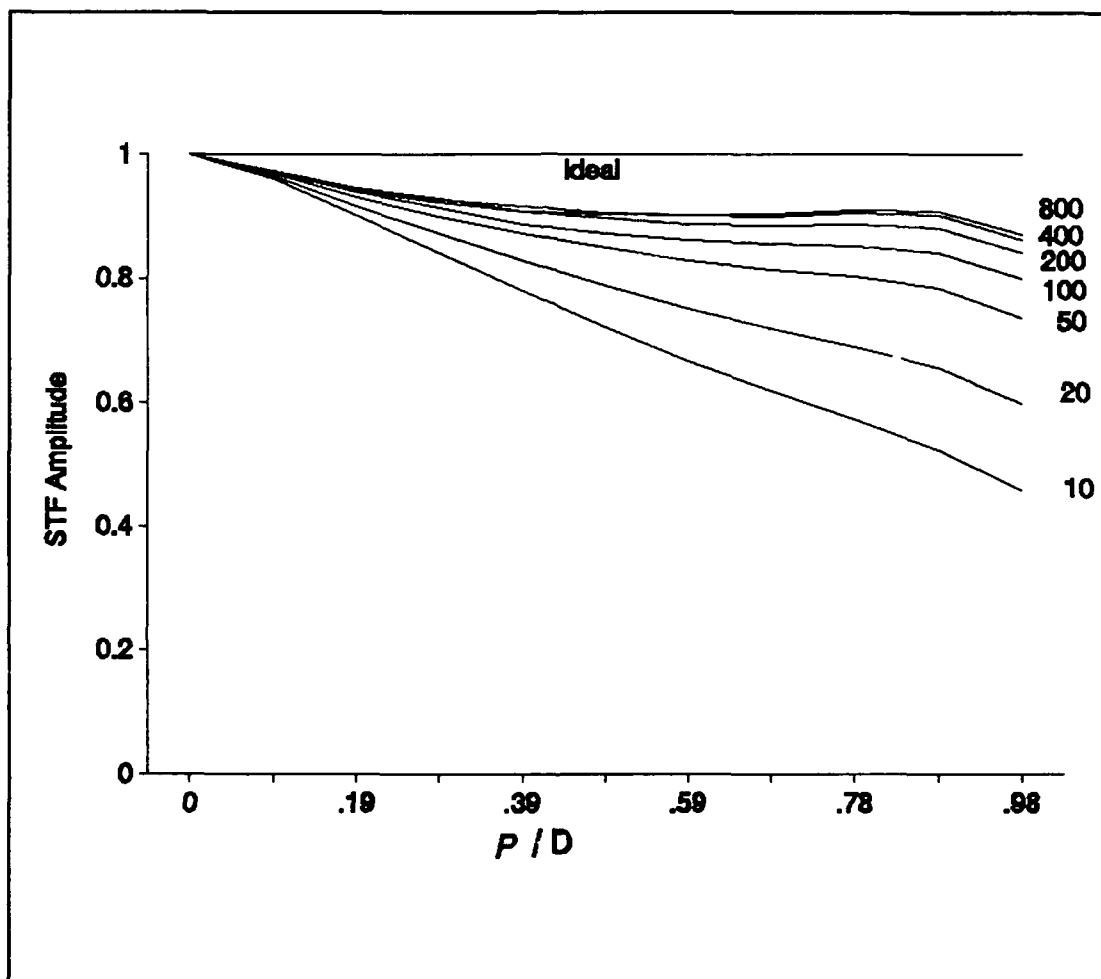


Fig. 14 STF for the subaperture photon count ranging from 10 to 800. Other parameters are constant $D = 2L$, and $L = 1/2 r_o$.

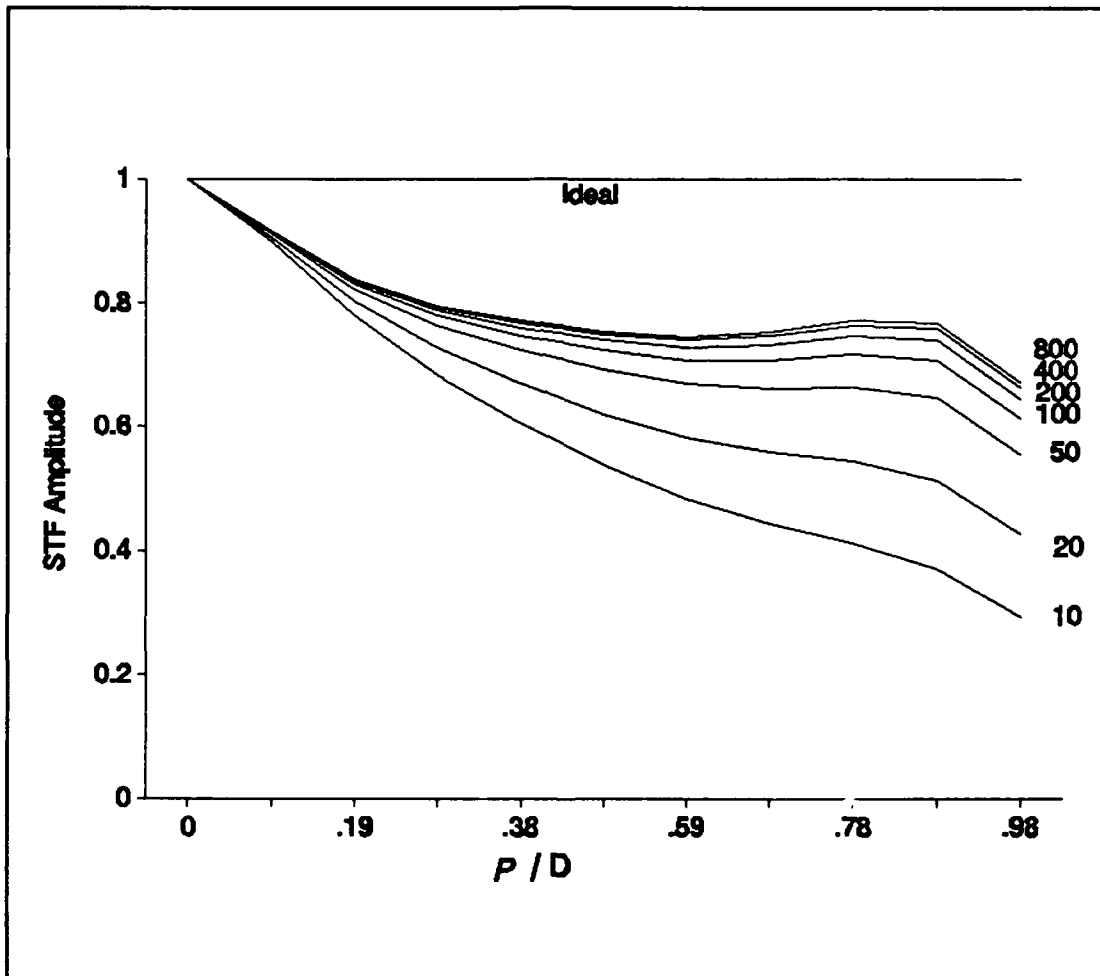


Fig. 15 STF for the subaperture photon count ranging from 10 to 800. Other parameters are constant $D = 2L$, and $L = 1 r_o$.

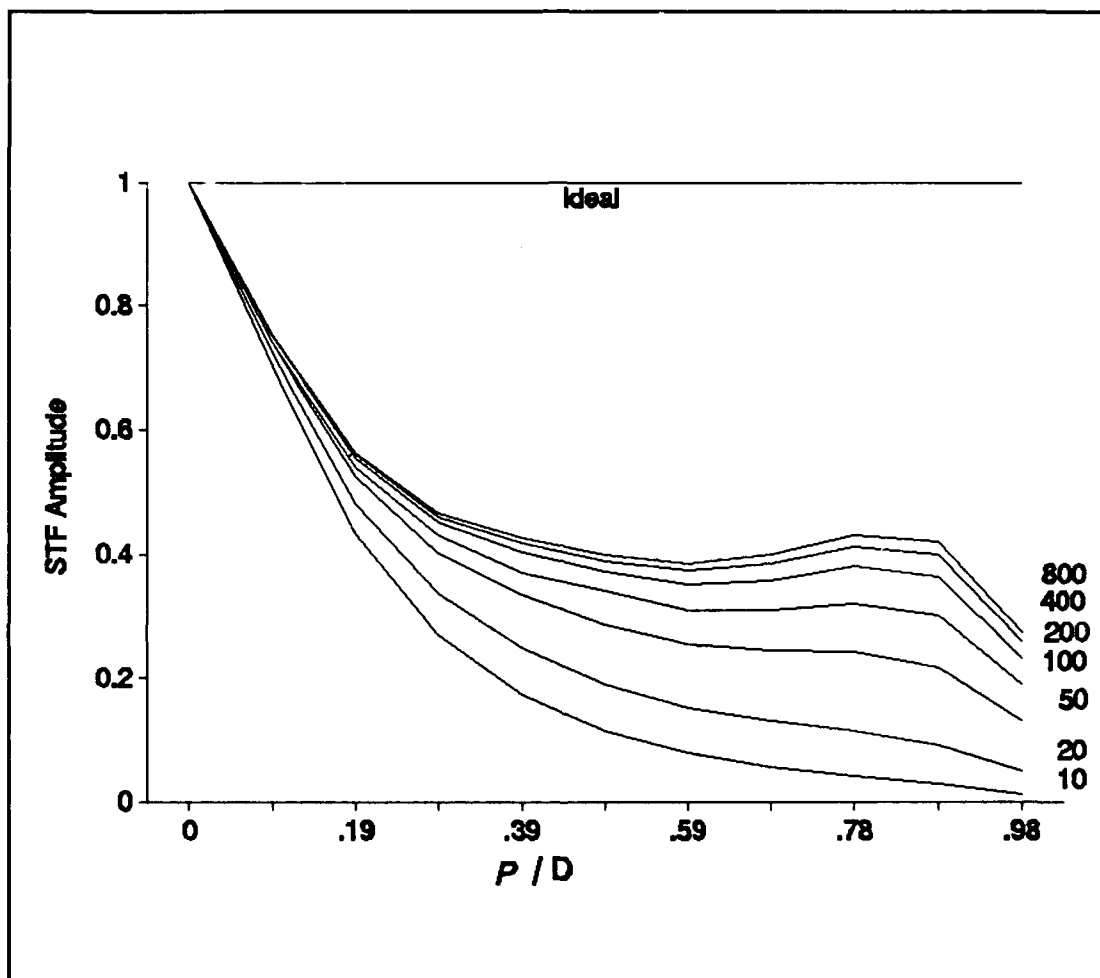


Fig. 16 STF for the subaperture photon count ranging from 10 to 800. Other parameters are constant $D = 2L$, and $L = 2 r_o$.

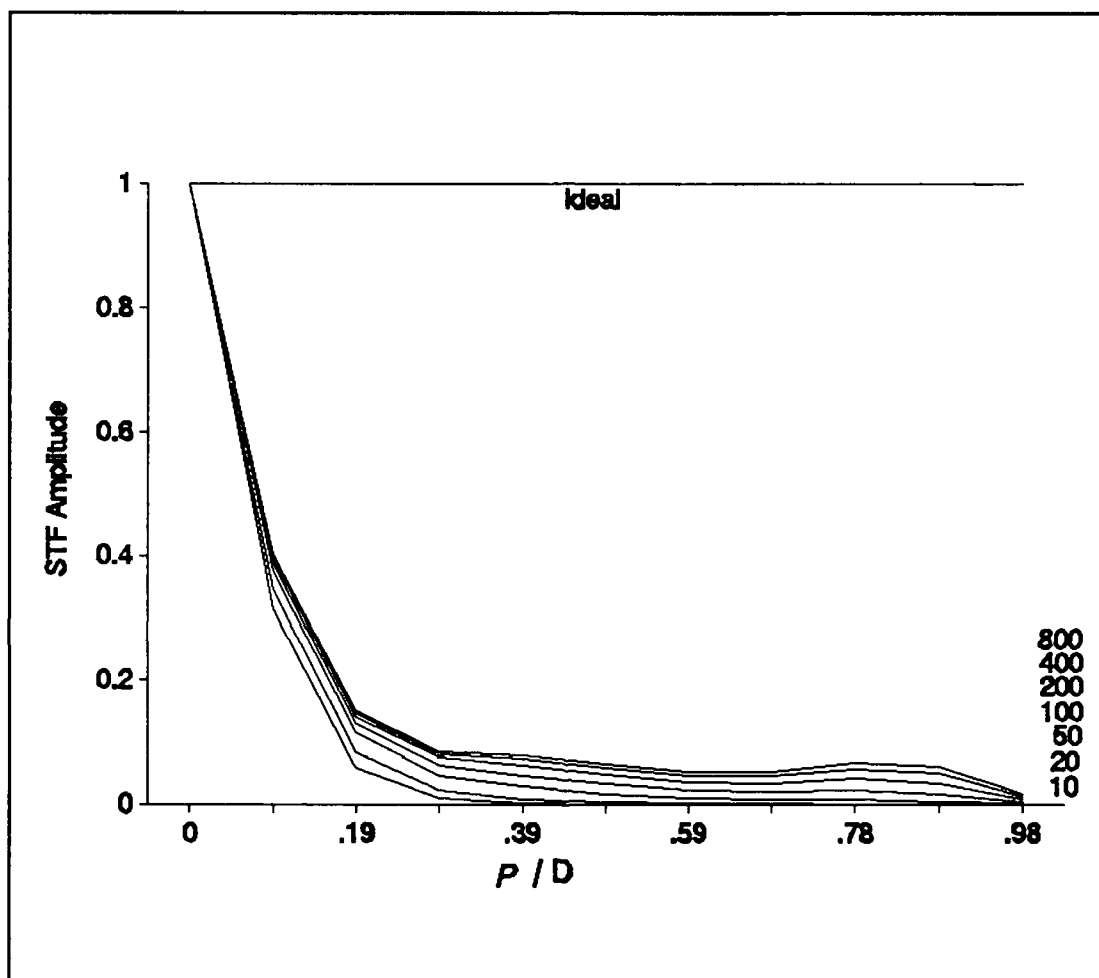


Fig. 17 STF for the subaperture photon count ranging from 10 to 800. Other parameters are constant $D = 2L$, and $L = 4 r_o$.

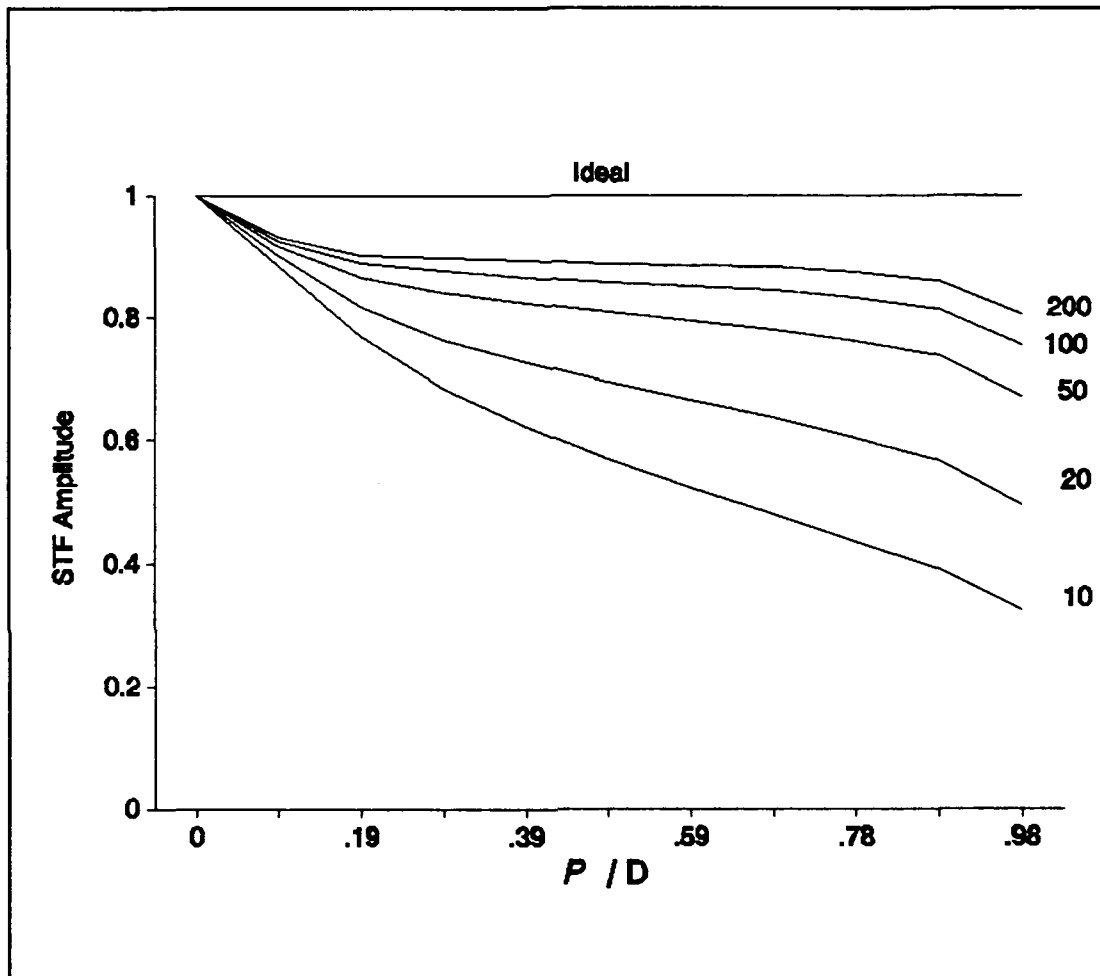


Fig. 18 STF for the subaperture photon count ranging from 10 to 200. Other parameters are constant $D = 5L$, and $L = 1/2 r_o$.

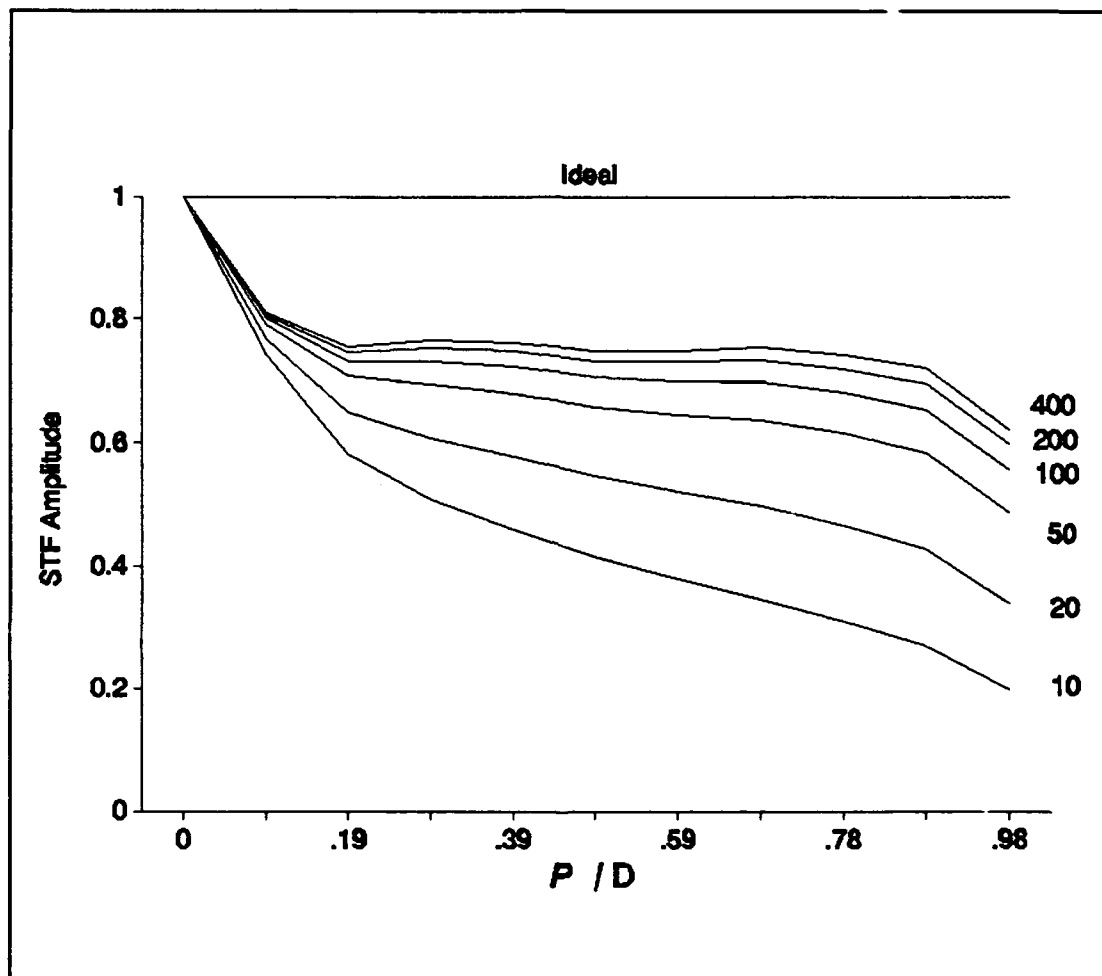


Fig. 19 STF for the subaperture photon count ranging from 10 to 400. Other parameters are constant $D = 5L$, and $L = 1 r_o$.

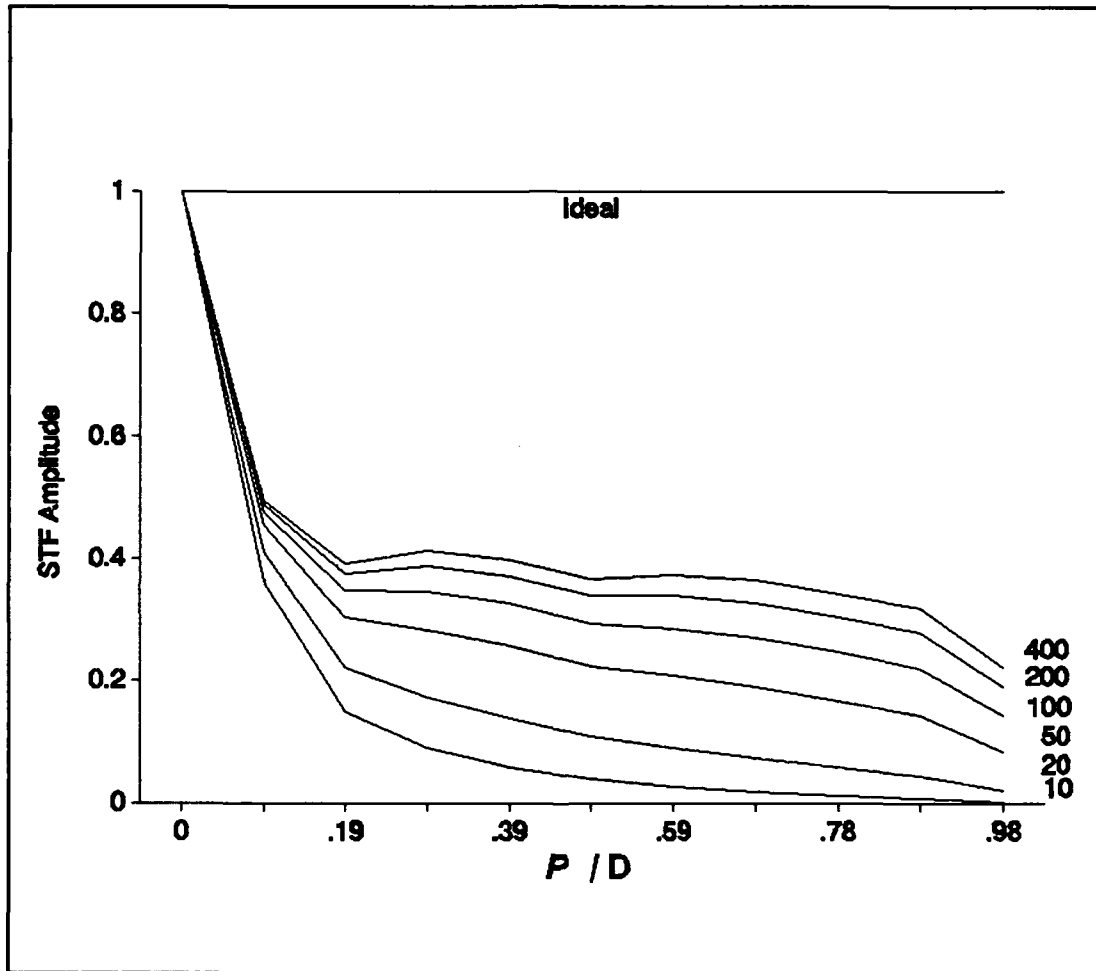


Fig. 20 STF for the subaperture photon count ranging from 10 to 400. Other parameters are constant $D = 5L$, and $L = 2 r_o$.

4.8 *Variation in Ratio of Subaperture to Atmospheric Coherence Diameter*

The results provided in this section are the effect on the STF of changing L/r_0 . Of the two parameters, this parameter is very important in defining the system and the effect on the system response. The results illustrate the advantage of sampling the wave front with an increasing number of subapertures. Ratios of L/r_0 of 0.5 and less approach the idealized system response. Results for both the 2 x 2 and the 5 x 5 sensor configurations are provided. Figure 21 depicts the results of varying L/r_0 for a 2 x 2 sensor configuration while holding the other parameters constant. The results shown in figure 22 were derived for a 5 x 5 sensor configuration and were obtained from the CRAY.

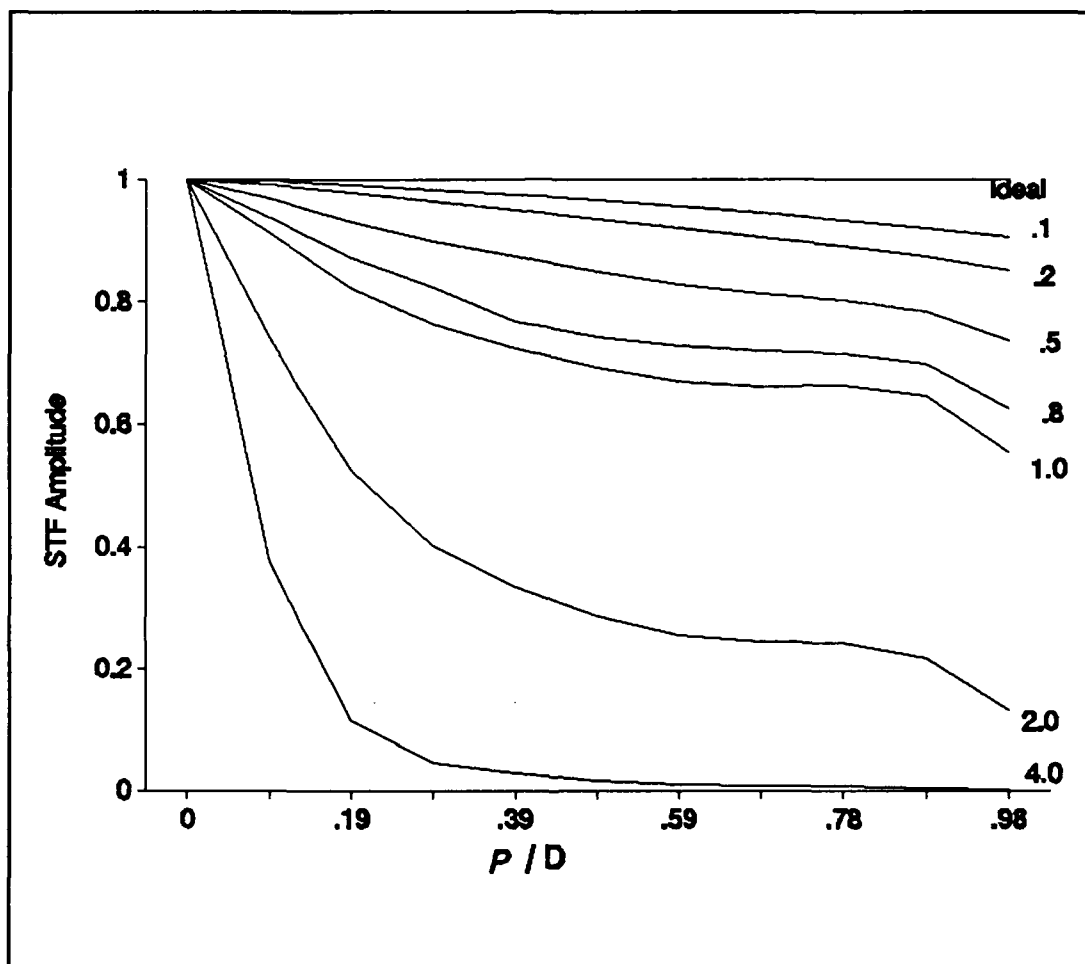


Fig. 21 STF for $L/r_o = .1$ to 4. Other parameters are constant $D = 2 L$, and photon count = 50

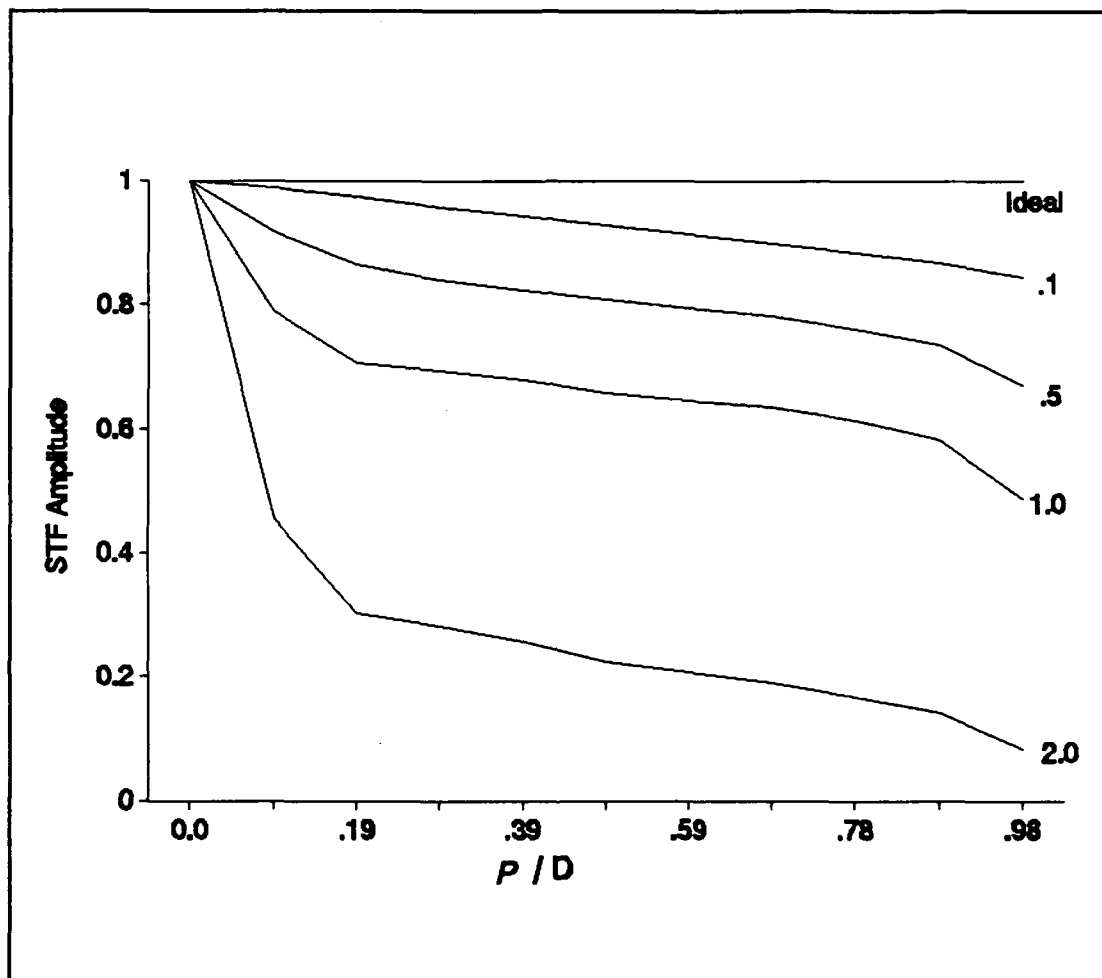


Fig. 22 STF for $L/r_o = .1$ to 2. Other parameters are constant $D = 5 L$, and photon count = 50

4.9 *Variation in Number of Subapertures*

To determine the applicability of representing larger sensor configuration arrays by smaller arrays, this section investigates the response of the STF algorithm to the variation of the number of subapertures while holding L/r_0 and N , the photon count constant. This capability to analyze large wave front sensor arrays is important. To perform the STF numerical analysis of large arrays would take thousands of hours on a computer. For the two parameters in this thesis, the ratio of subaperture size to atmospheric coherence diameter and photon count per subaperture, numerical results were obtained for increasing number of subapertures while holding the other parameters constant. If consistency in the results is maintained this permits an analysis of larger sensor configurations using representative smaller arrays that are computationally possible. The sensor configurations of 2×2 , 3×3 , 4×4 , and 5×5 were analyzed for a fixed L/r_0 and a photon count of $N = 100$. The four configurations, and corresponding results are shown in figure 23. As can be observed, the results track very well leading to the conclusion that large arrays may be analyzed by smaller array configurations for these two key parameters, L/r_0 and photon count.

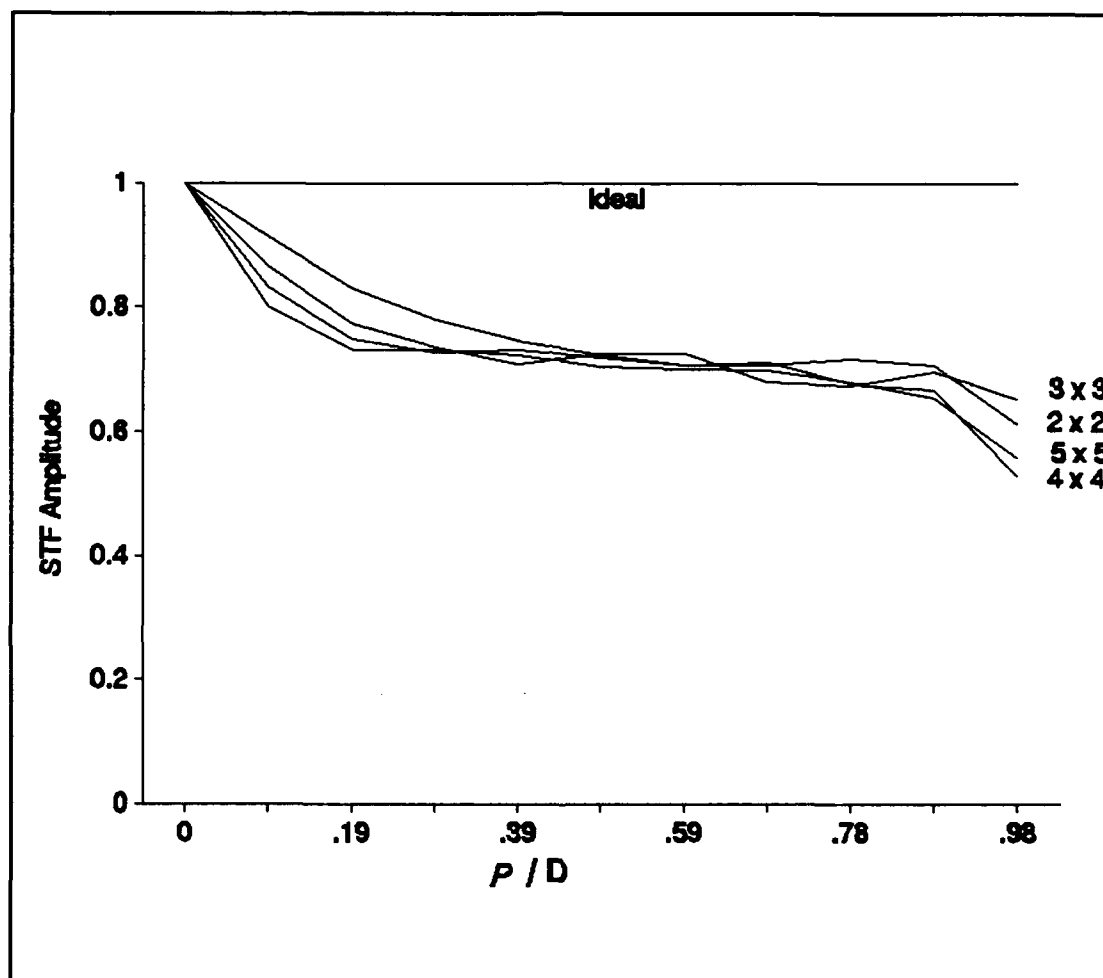


Fig. 23 STF for changes in the sensor configuration $D = 2, 3, 4, 5L$. Other parameters are constant $r_o = 1$, and photon count = 100.

4.10 System Spread Function

For the purpose of this thesis, the system spread function (SSF) is defined as the Fourier transform of the system transfer function (STF) where $O(\rho)$ is the STF. The STF and SSF relationship is similar to the OTF and PSF presented by Welsh (4:1920). The system spread function entails the atmospheric phase screen, the telescope, the wave front sensor, and the wave front reconstructor. The relationship is as follows (4:1920)

$$\langle s(u/\lambda f_D, v/\lambda f_D) \rangle = \frac{F_2^{-1}[\langle O(\rho) \rangle]}{(\lambda f_D)^2} \quad (40)$$

For comparison the point spread function becomes an idealized sinc squared function while the system spread function for the ideal case will be a sinc function. For low photon counts and large L/r_o the SSF attempts to resemble a sinc function while at high photon counts and small L/r_o values the SSF in fact approaches a sinc function. As depicted in figure 24 the system spread function does approach the ideal for small L/r_o values and large photon counts. System spread functions are presented for both the 2 x 2 and 5 x 5 sensor configurations. The varying parameter will be photon count while the other parameters are held constant for figures 24 - 28. For figure 29 the varying parameter will be L/r_o .

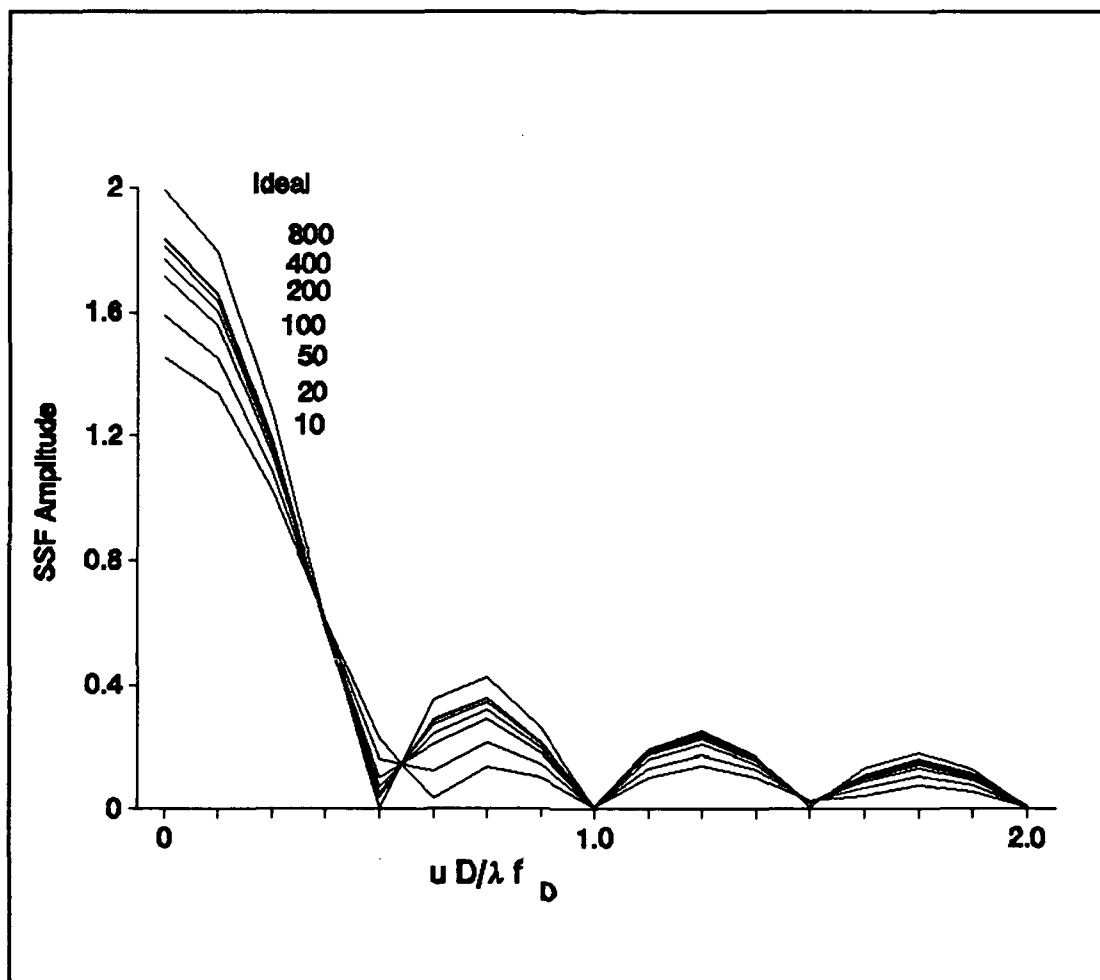


Fig. 24 System spread function for the subaperture photon count ranging from 10 to 800. Other parameters are constant $D = 2 L$, and $L = 1/2 r_o$.

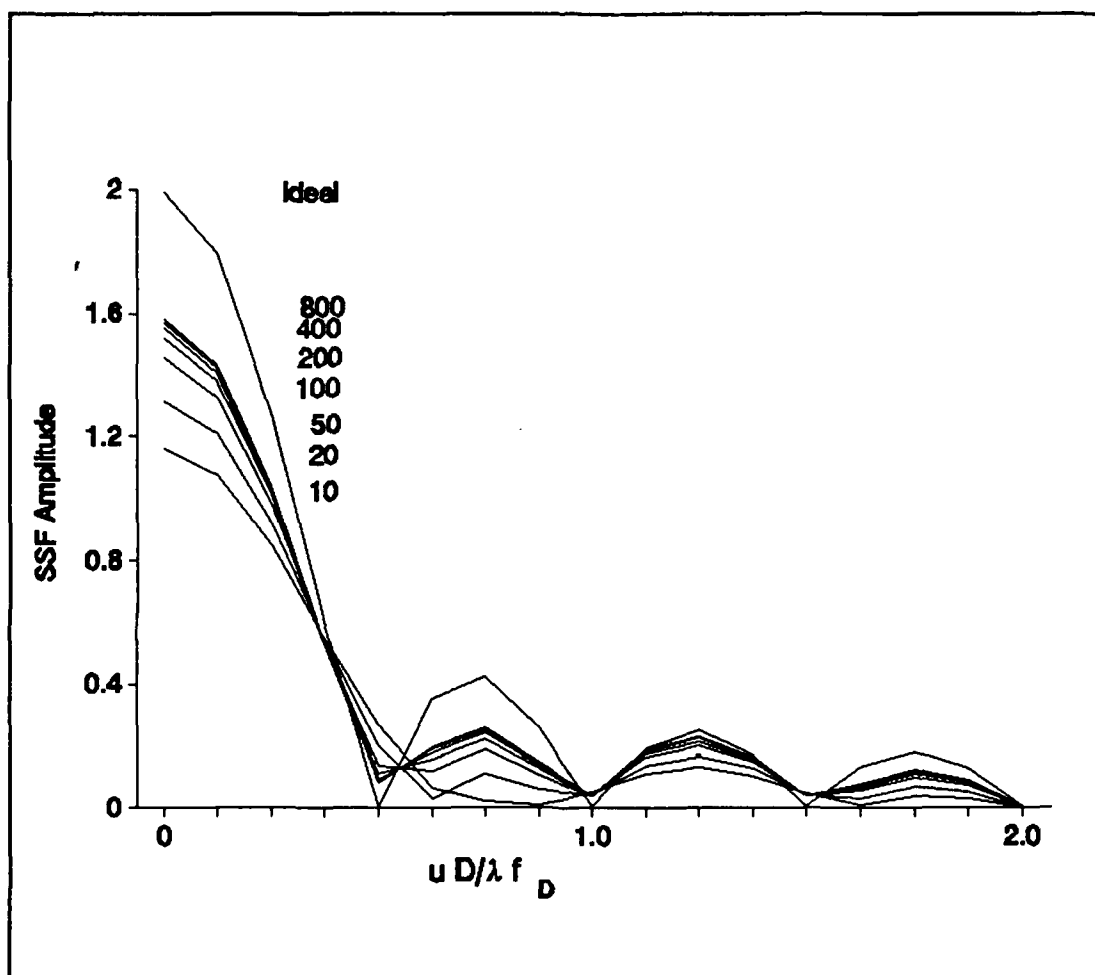


Fig. 25 System spread function for the subaperture photon count ranging from 10 to 800. Other parameters are constant $D = 2L$, and $L = 1 r_o$.

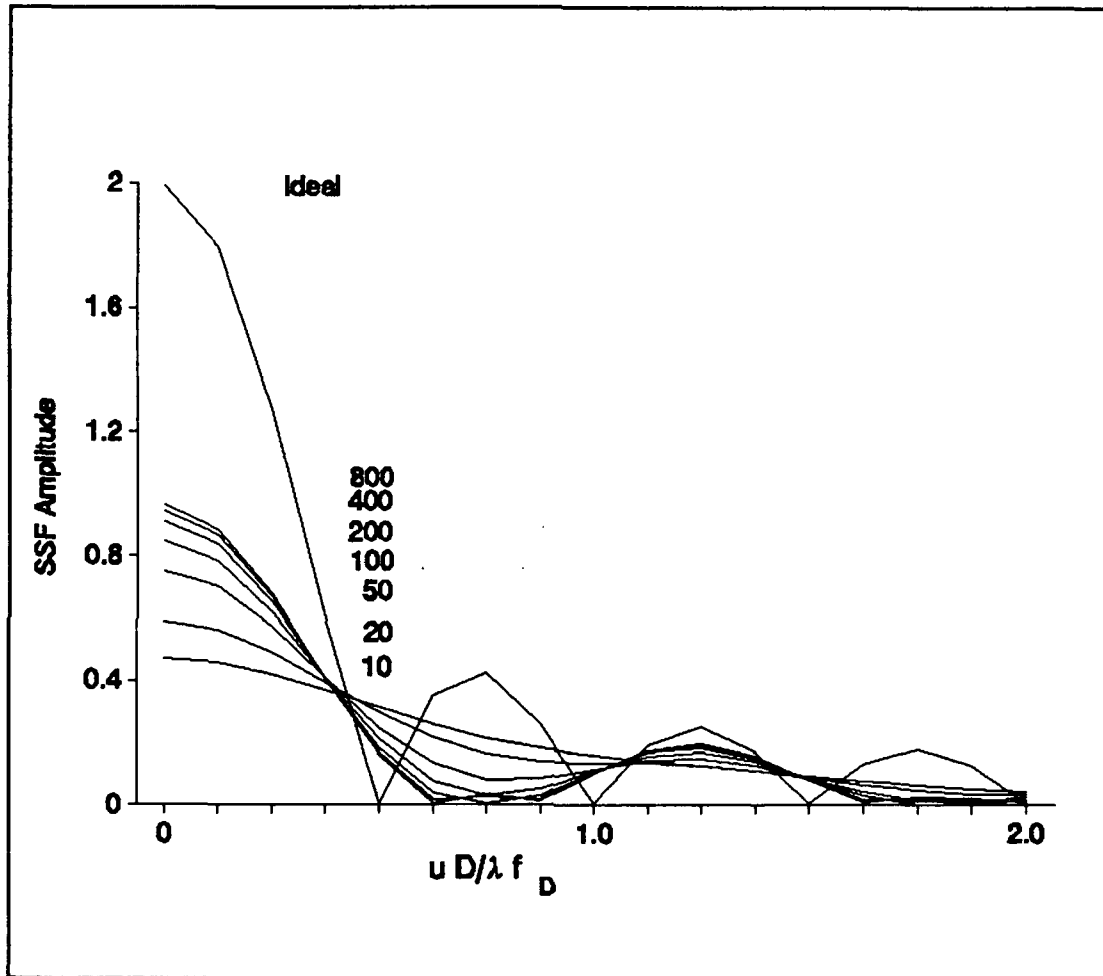


Fig. 26 System spread function for the subaperture photon count ranging from 10 to 400. Other parameters are constant $D = 2 L$, and $L = 2 r_o$.

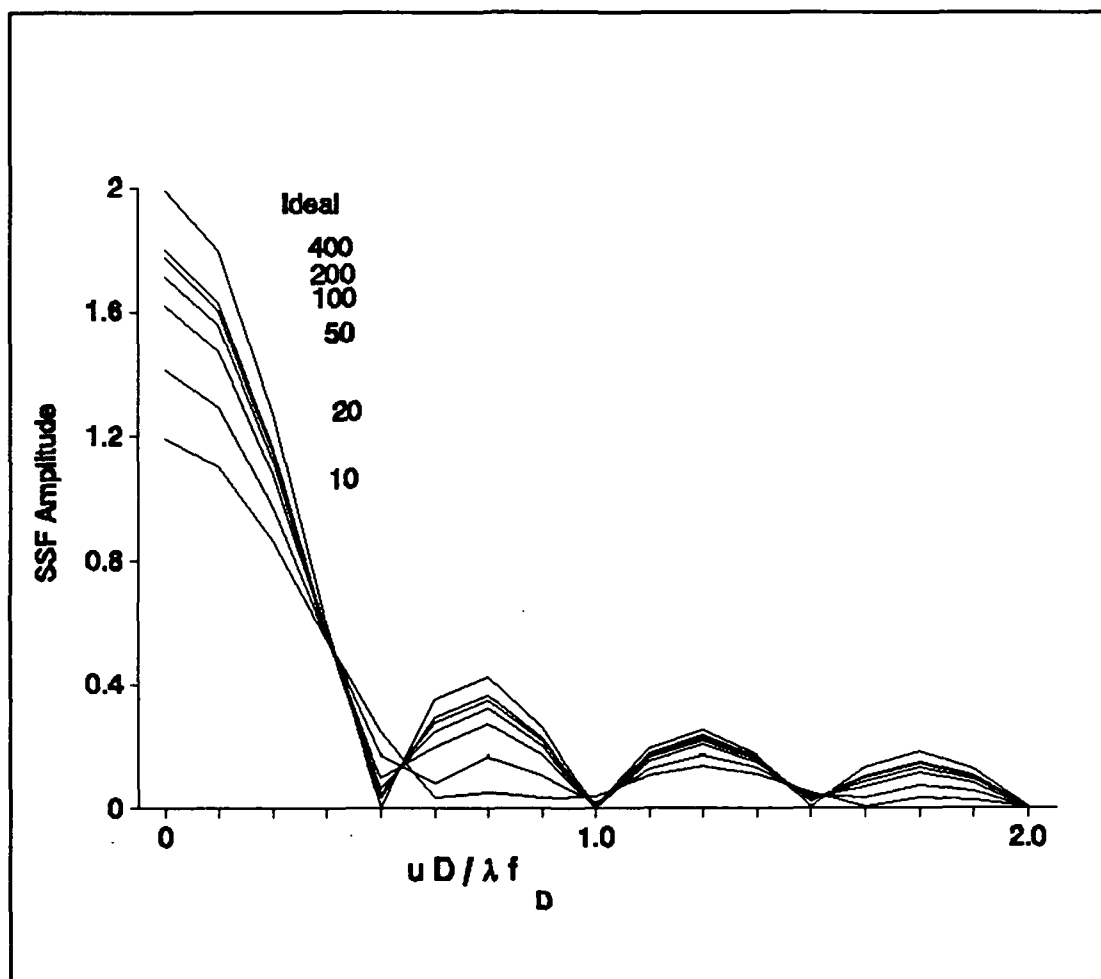


Fig. 27 System spread function for the subaperture photon count ranging from 10 to 400. Other parameters are constant $D = 5 L$, and $L = 1/2 r_o$.

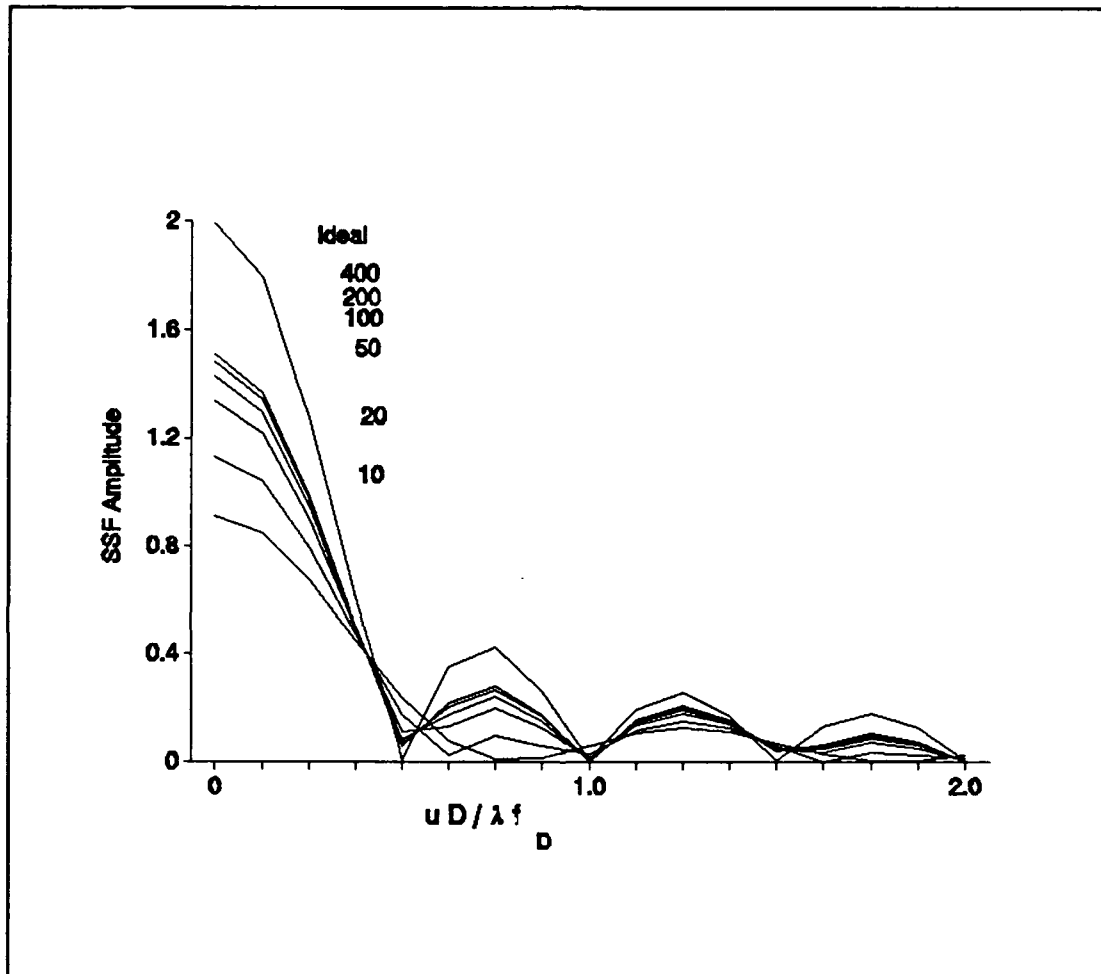


Fig. 28 System spread function for the subaperture photon count ranging from 10 to 400. Other parameters are constant $D = 5 L$, and $L = 1.0 r_o$.

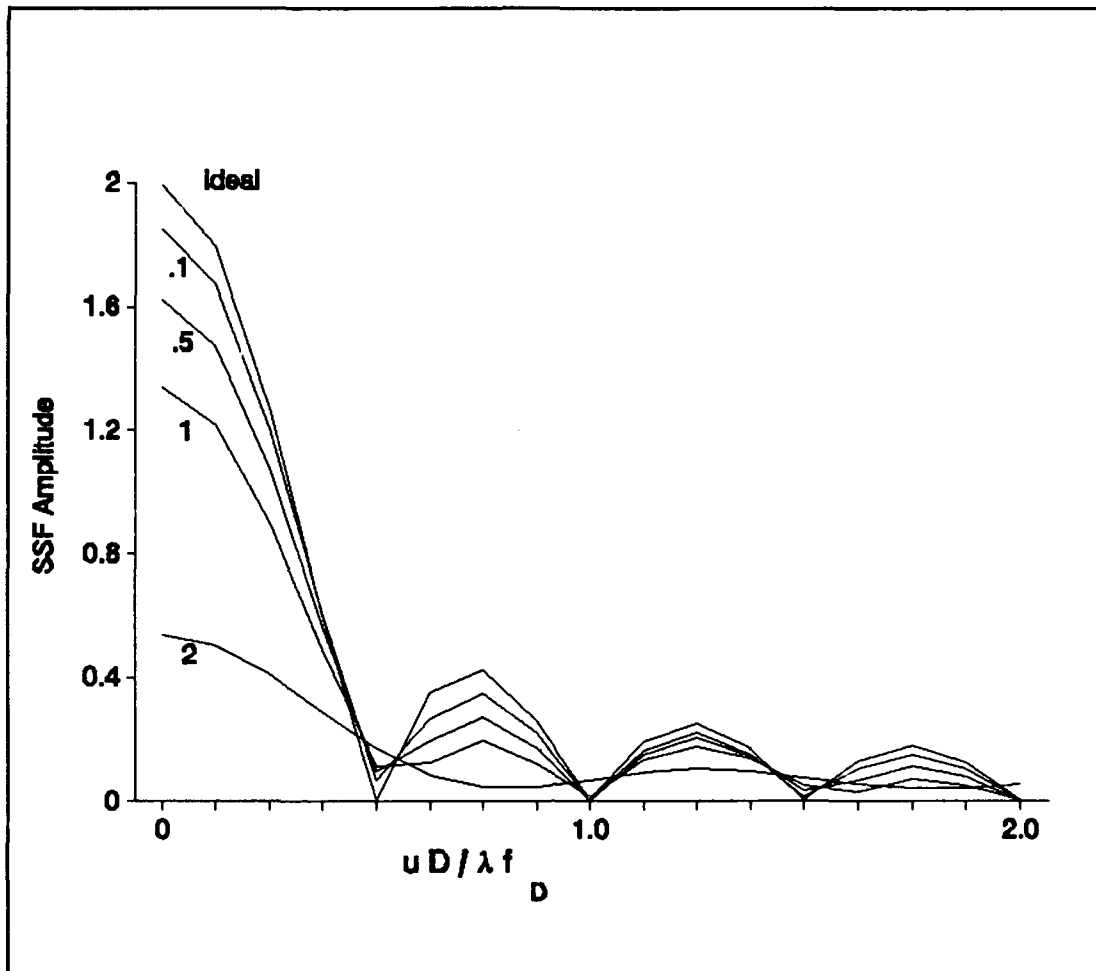


Fig. 29 System spread function for changing subaperture size to r_0 ratio. Other parameters are constant $D = 5 L$, and photon count = 50.

4.11 *System Strehl Ratio*

For this thesis the system Strehl ratio is defined as the maximum amplitude of the system spread function versus the maximum amplitude of the ideal system spread function. The system Strehl ratio for several of the cases is shown in figures 30 through 32. As in the case of Welsh's analysis of the optical transfer function, the system Strehl ratio is improved with decreasing subaperture size (4:1921).

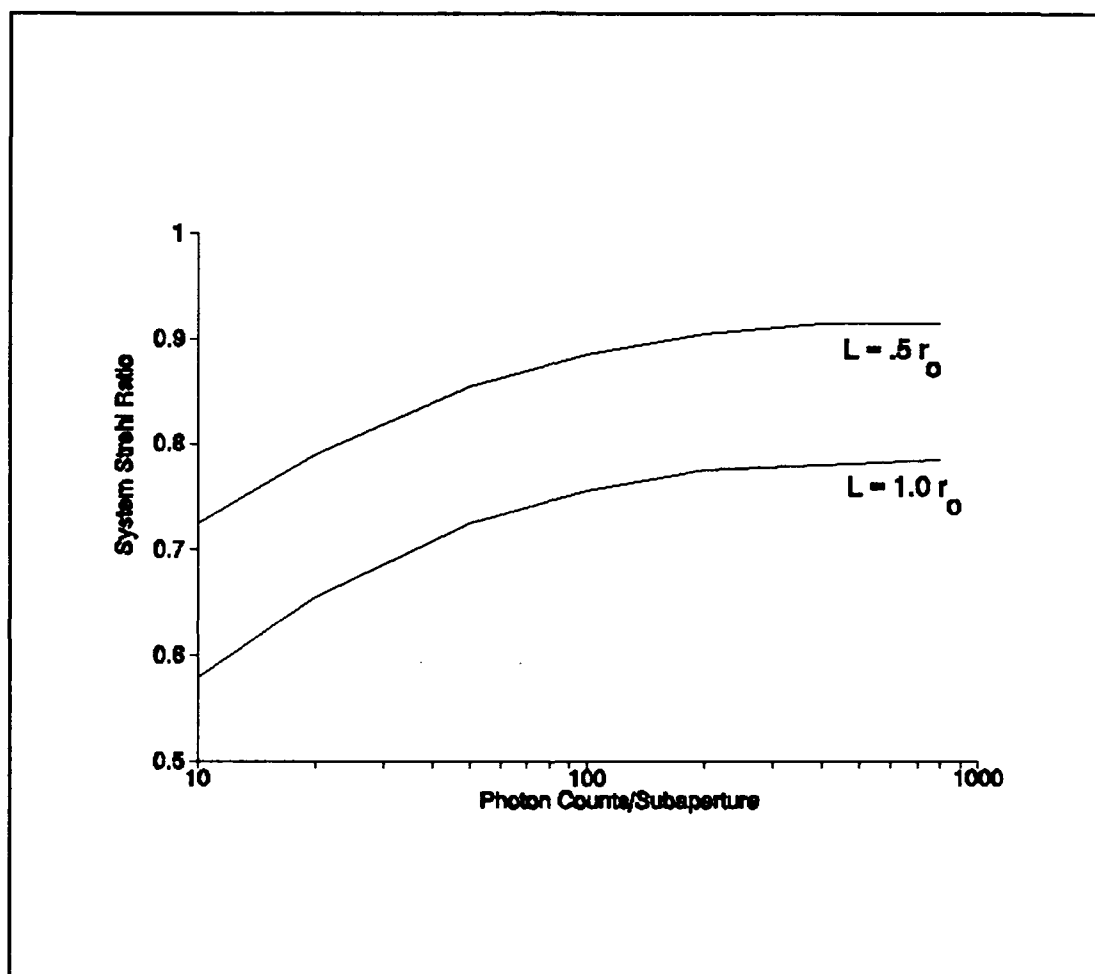


Fig. 30 System Strehl ratio versus subaperture photon count. Two plots are shown for $D = 2 L$, and $L = 1/2$ and $L = 1 r_0$.

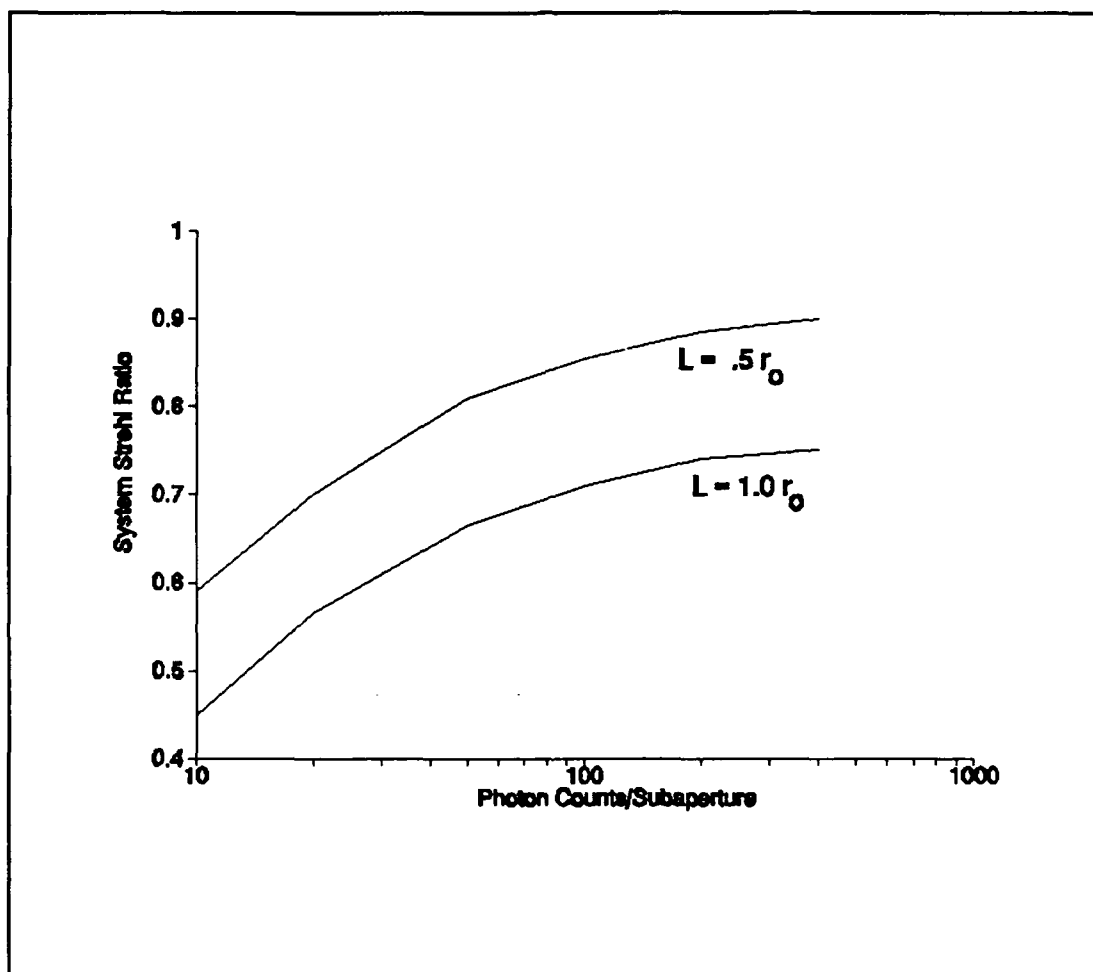


Fig. 31 System Strehl ratio versus subaperture photon count. Two plots are shown for $D = 5 L$, and $L = 1/2$ and $L = 1 r_0$.

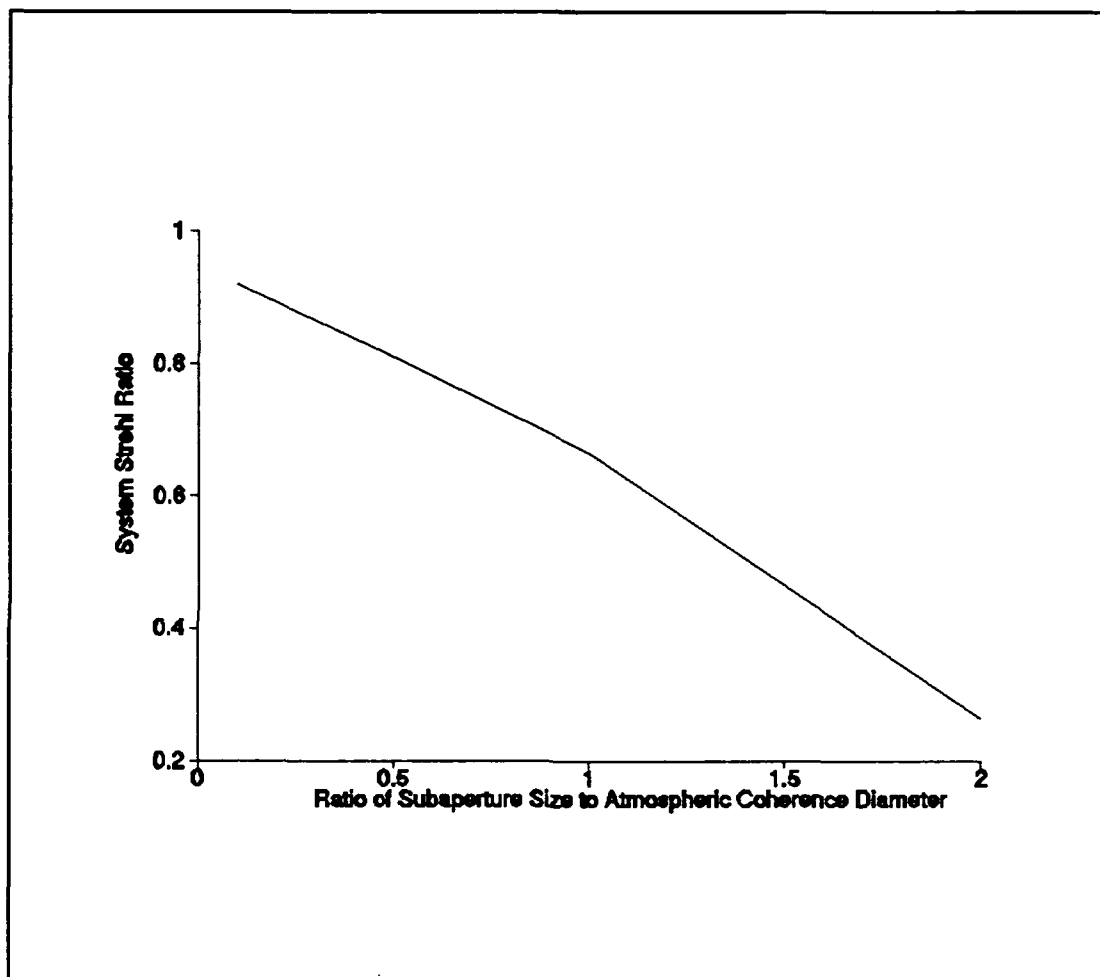


Fig. 32 System Strehl ratio versus ratio of subaperture size to atmospheric coherence diameter r_0 . Other parameters are constant $D = 5 L$, and photon count = 50.

4.11 *Performance Analysis of the Air Force Phillips Laboratory Atmospheric Compensation Experiment.*

The STF algorithm allows an analysis of the experimental setup used by the Air Force Phillips Laboratory for the image compensation of α Aurigae (Capella). To obtain the subaperture size of the wave front sensor an analysis of the experiment was performed. To obtain the photon count incident on the wave front sensor subaperture this thesis obtained information from the Air Force Phillips Laboratory on the calculated photon flux per subaperture. For the subaperture size, the aperture diagram with the wave front sensor optically conjugate is shown in figure 33. As shown the subaperture size of the wave front sensor is roughly .7 cm. The photon count per subaperture is 1221 photons. The atmospheric coherence factor, r_0 was estimated by the Phillips Lab to be at 7 cm (2:4529). With the subaperture size at approximately .7 cm, the ratio of subaperture size L to r_0 is about .1. A plot of photon incidence of 1221 and a L/r_0 ratio of .1 is shown in figure 34 with the corresponding system spread function shown in figure 35. The STF results for decreasing photon flux is shown in figure 36. As shown in figure 34, the claim by the Air Force Phillips Laboratory that diffraction limit resolution was achieved can be substantiated by the numerical analysis of their experiment by the system transfer function algorithm. The amplitude of the higher spatial frequencies are boosted to over 90% of the amplitude of the lower spatial frequencies. The system Strehl ratio was calculated to be .98.

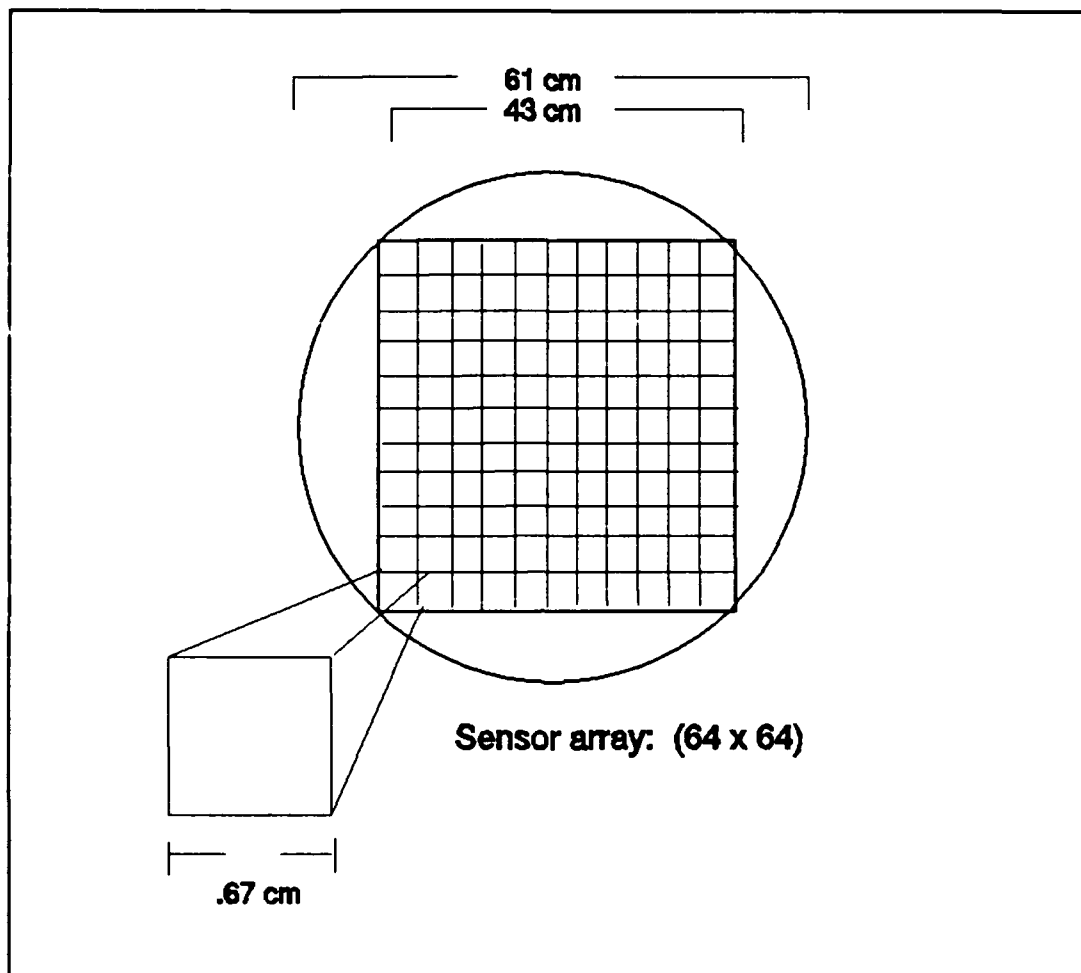


Fig. 33 Squaring of imaging aperture and sensor configuration for the Air Force Phillips experiment performance analysis.

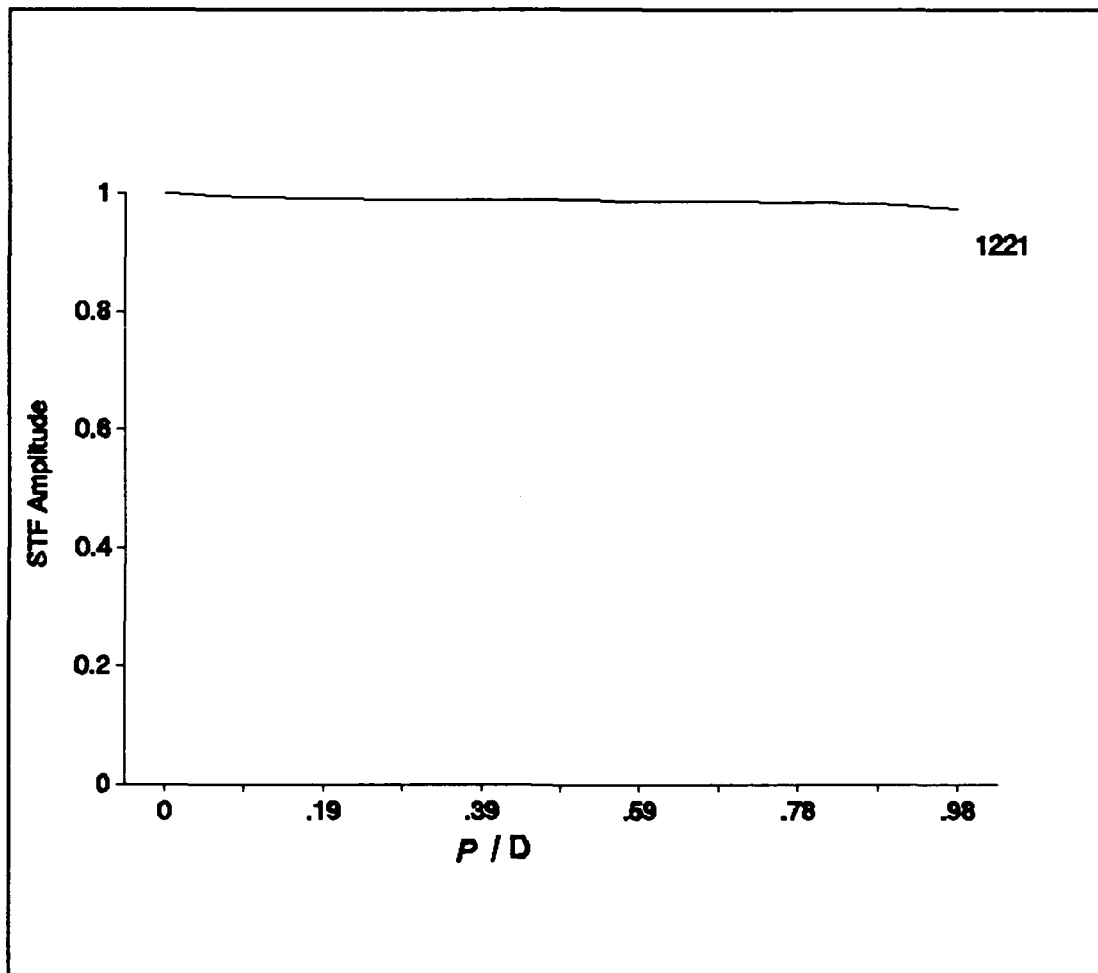


Fig. 34 STF performance analysis of the Air Force Phillips experiment. Photon count is 1221 per subaperture. The L/r_o is .1. A 5 x 5 sensor configuration was used to obtain the plotted data.

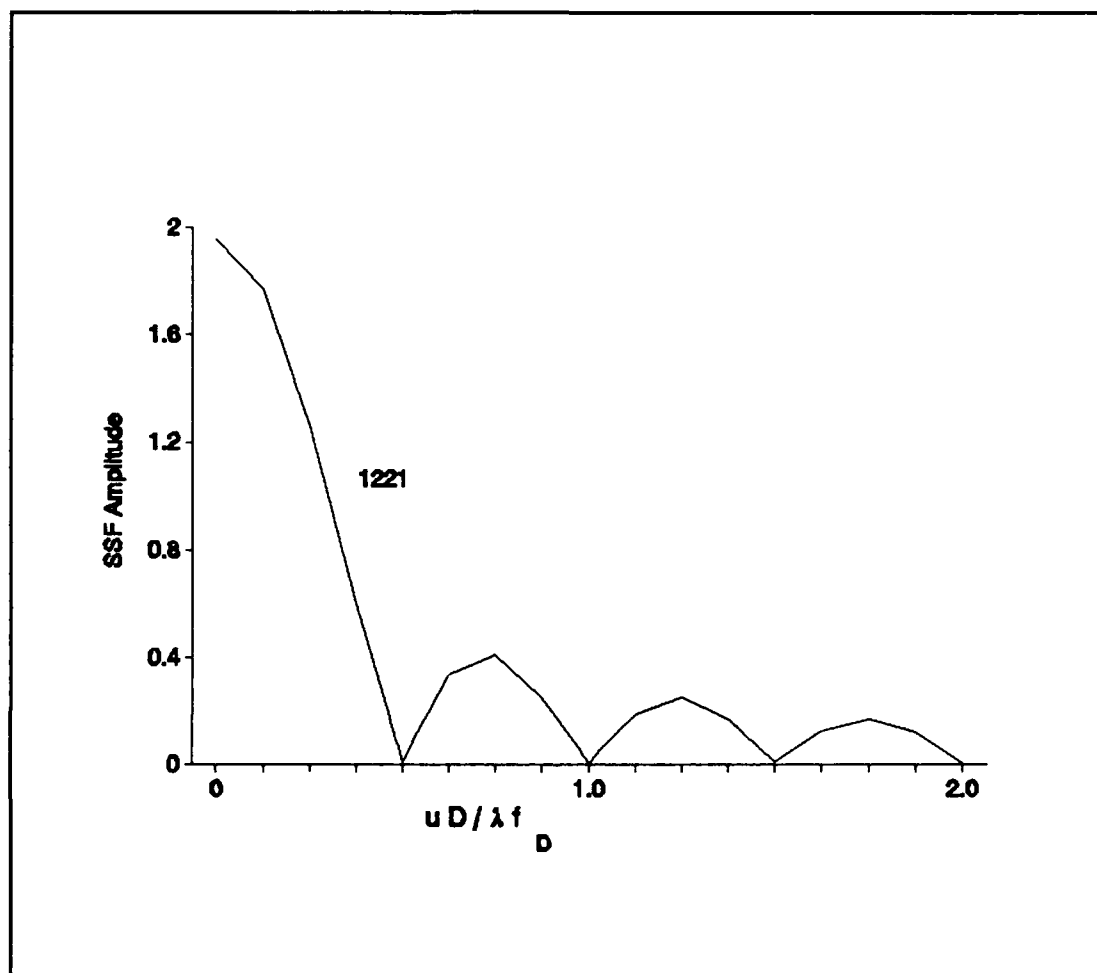


Fig. 35 SSF performance analysis of the Air Force Phillips experiment. Photon counts is 1221 per subaperture. The L/r_0 is .1. A 5 x 5 sensor configuration was used to obtain the plotted data.

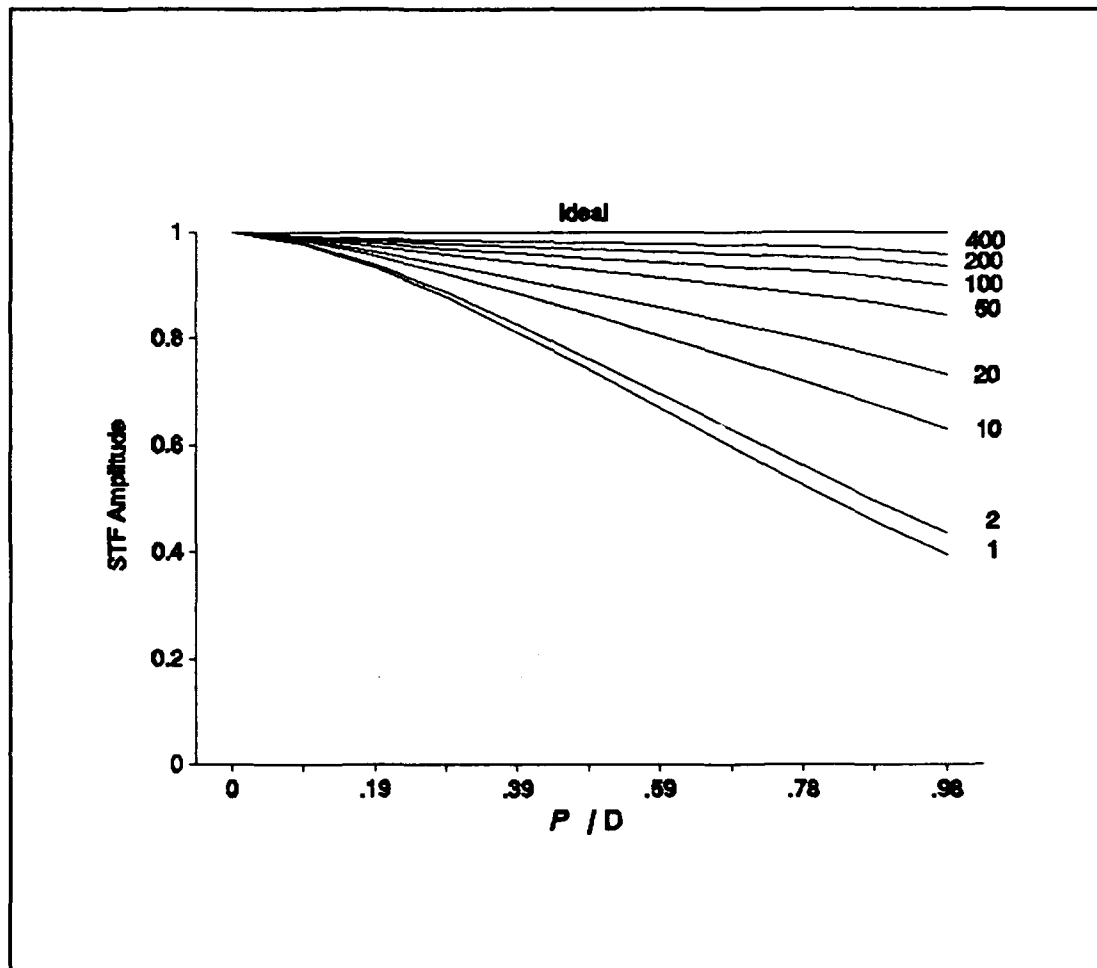


Fig. 36 STF performance analysis of the Air Force Phillips experiment. Photon count is varies from 1 to 400 counts per subaperture. The L/r_o is .1. A 5 x 5 sensor configuration was used to obtain the plotted data.

V. Conclusions and Recommendations

Chapter I described the stellar speckle phenomena and methods of obtaining high resolution images in spite of atmospheric turbulence effects. Chapter II presented a short synopsis of the literature on the stellar speckle phenomena and a synopsis of the Phillips Laboratory speckle holography experiment. Chapter III presented the derivation of a system transfer function from background theory and models using a square telescope aperture, a wave front sensor and a wave front reconstructor. Chapter IV presented the numerical results obtained. This chapter provides contributions of this thesis, key elements and recommendations for further study.

5.1 Thesis Contributions

Previous efforts were limited to the analysis of the optical transfer function. This effort addressed and analyzed the response of the system. The software developed allows a quantitative analysis of the wave front sensor configuration. A figure of merit can be assigned to a wave front sensor configuration design based on the parameter inputs of photon incidence, atmospheric coherence diameter, and subaperture size. This will allow an optimized wave front sensor configuration.

5.2 Key Elements

After review of the data obtained, this thesis reiterates the key contribution of the sensor subaperture size. Though the photon incidence per subaperture and sensor subaperture size are interrelated, if there is sufficient photon energy for the wave front sensor, reductions in the size of the subaperture improve the resolution. Subaperture size to r_0 ratios of less than .5 greatly improve the resolution over higher ratios. The experiment of the Air Force Phillips Laboratory in the imaging of α Aurigae (Capella) with a L/r_0 ratio of .1 produced a nearly diffraction limited resolution. The claim by the Phillip's laboratory of nearly diffraction resolution is reinforced by the numerical results

of this thesis.

5.3 Additional Analysis

Continued interest in the analysis of the wave front sensor optimization would be the basis for a variance analysis of the averages of the optical transfer function. This effort would be computer intensive. Where as the code developed for this analysis required a four-fold integral a variance analysis may require an eight-fold integral, a computationally time intensive program.

Bibliography

1. Hardy, John W., "Active Optics: A New Technology for the Control of Light," *Proceedings of the IEEE* 66: 6: 651-697 (June 1978)
2. Gonglewski, John D., D. G. Voelz, J. S. Fender, D. C. Dayton, B. K. Spielbusch, and R. E. Pierson, "First Astronomical Application of Postdetection Turbulence Compensation: Images of Aurigae, Ursae Majoris and Geminorum Using Self-Referenced Speckle Holography," *Applied Optics* 29: 31: 4527-4529 (1 November 1990).
3. Foley, Theresa M., "Air Force Building High-Resolution Telescope for Space Defense Research," *Aviation Week and Space Technology*, p. 47, (6 March 1989).
4. Welsh, Byron M. and Chester S. Gardner, "Performance Analysis of Adaptive-Optics Systems Using Laser Guide Stars and Slope Sensors," *Journal of the Optical Society of America* 6: 12: 1913-1923 (December 1989).
5. Dainty, J.C., *Laser Speckle and Related Phenomena*, (Springer-Verlag Berlin Heidelberg, New York, 1975) p. 255-280.
6. Primot, J., G. Rousset, and J.C. Fontanella, "Deconvolution From Wave-Front Sensing: a New Technique for Compensating Turbulence-Degraded Images," *Journal of the Optical Society of America* 7: 9: 1598-1608 (September 1990).
7. Wallner, Edward P., "Optimal Wave-Front Correction Using Slope Measurements," *Journal of the Optical Society of America* 73: 12: 1771-1776 (December 1983).
8. Goodman, Joseph W., *Statistical Optics*, (Wiley, New York, 1985) p. 20.
9. Kane, T. J., B. M. Welsh, C. S. Gardner, and L. A. Thompson, "Wave Front Detector Optimization for Laser Guided Adaptive Telescopes," *Active Telescope Systems, Proc. Soc. Photo-Opt. Instrum Eng.* 1114:160-171 (1989).
10. Fried, D. L., "Optical Resolution Through a Randomly Inhomogeneous Medium for Very Long and Very Short Exposures," *Journal Optical Society of America* 56: 1372-1379, (1966)